Chapter 4

Brush-Induced Macroscopic Alignment of Self-Assembling Peptide Nanofibers: Potential Therapeutic Lead for Regeneration in Sciatic Nerve Injury

4.1 ABSTRACT

The consequences of peripheral nerve damage can cause painful neuropathies and impairments. Successful fascicular rearrangement of an injured peripheral nerve necessitates the reconnection of nerve sprouts from the anterior and Büngner bands from the distal sides of the lesion. The current gold standard for nerve transplantation is autogenous nerve grafting. However, the current neural scaffolds have restricted neuroregeneration efficacy due to either the absence of fiber alignment and a conductive second phase, resulting in impaired electrical conductivity, or the absence of extracellular matrix components. A multitude of tissue engineering nerve-guiding conduits have been devised as alternatives to autografts. Yet, only a small number of conduits can produce the same reparative effect as autografts. Here, we report the design and development of a nanofibrous ECM mimicking self-assembling peptide hydrogel containing a neuroregenrative motif (NAP and NAV) to enhance neurite outgrowth and a self-assembling motif ($K_2(SL)_6K_2$). We observed that the nanoscale topographic characteristics of this hydrogel played a crucial role in directing the cell orientation of stem cells. Upon application of these peptide nanofibers as a nerve growth control to rectify the sciatic nerve deficit in rats, a successful restoration of the nerve defect was seen within 2 weeks. Following a 2-week period, we found that the peptide hydrogel successfully facilitated structural repair and functional recovery. This was confirmed by morphological and histological analyses, functional studies, and evaluations of gastrocnemius muscle reinnervation. This suggests that this peptide hydrogel successfully facilitated the regeneration and restoration of nerve function. In conclusion, the peptide nanofibrous hydrogel shows significant promise in the management of sciatic nerve injury.

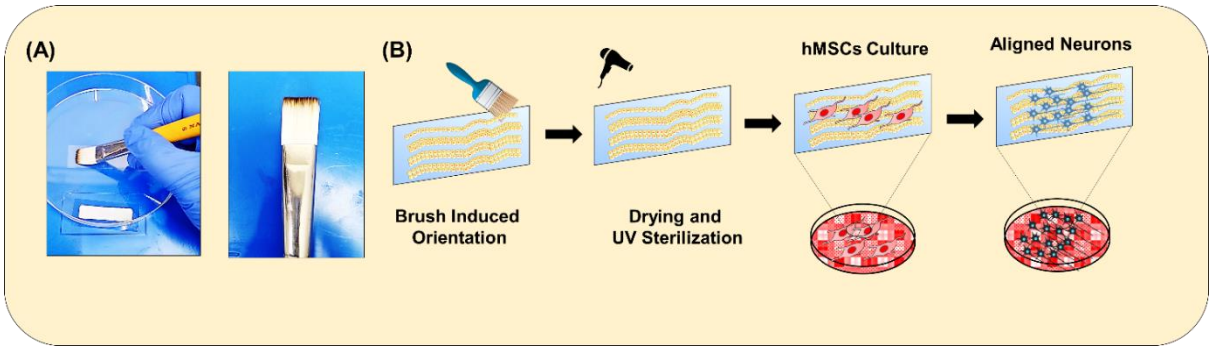


Figure 4.1 (A) Experimental arrangement for manual brushing utilising a nylon paintbrush. (B) Schematic illustration of the aligned peptide hydrogel.

4.2 INTRODUCTION

The clinical problem of sciatic nerve injury (SNI) is of utmost importance worldwide. Around one million SNI occur globally per year, resulting in severe impairment of sensory and motor nerves, leading to loss of function and even impairments, therefore significantly impacting the quality of life for affected individuals.[1–3] SNIs are mainly caused by severe or penetrating trauma or sudden compression, resulting in the impairment of motor function, sensory function, or both. Within the current clinical practice, tensionless epineural suturing is the present clinical treatment for small nerve gap deficit syndrome.[4,5] However, autografts continue to be the preferred method for repairing peripheral nerves in cases of long-distance abnormalities (>6 mm) where complete end-to-end reconnection is impossible.[6,7] However, their effectiveness is constrained by many issues, such as the absence of donor nerves, the development of neuromas, and the occurrence of secondary injuries. Suggesting immediate needs for the advancement of novel and efficient therapies.[8]

In recent years, many synthetic polymers like Poly(3,4-ethylenedioxythiophene), polyaniline and similar conductive polymers have been utilised in the construction of neural and other soft tissue scaffolds, including muscular, heart, and skin structures.[9,10] Researchers have also used a composite scaffold made of polydimethylsiloxane/polycaprolactone (PCL) to manipulate Schwann cells in SCI.[11] However, comprehensive verification is lacking to determine the appropriateness of these scaffolds in living organisms, considering their limited biodegradability. Further, the assessment of long-term biocompatibility and the corresponding safety measures were also inadequate[12]. Hence, the integration of conductive materials to enhance the electrical property of scaffolds is a preferable option for the ideal development of biocompatible materials for the recovery of SNI. [13]

Technological progress in molecular science has made substantial contributions to the fast-growing disciplines of bionanotechnology and the creation of innovative biomaterials. Peptide-based materials have demonstrated significant potential for biomedical applications due to their ability to replicate the structure and intricacy of the extracellular matrix (ECM), which is sometimes impaired or completely absent in cases of injury and disease.[14,15]

These materials can be specifically engineered to enhance the processes of cell adhesion, proliferation, and differentiation, rendering them as an ideal candidate for applications in tissue engineering and regenerative medicine.[16] Moreover, peptide-based materials have the capacity to achieve regulated release of bioactive compounds, therefore augmenting their therapeutic capabilities.[15,17] These materials can be specifically engineered to form hydrogels, which are highly water-dense crosslinked fibrous networks that replicate the physical structure of tissues. These hydrogels have many biomedical uses, including drug delivery, wound healing, and tissue regeneration. Hydrogels have an excellent inherent capacity to adjust their mechanical characteristics and degradation rates, rendering them very adaptable materials for imitating the extracellular matrix of various tissues in the human body.[18,19]

The self-assembling multidomain peptide (SAMDP) hydrogels in this chapter are formed by the molecular assembly of amphiphilic peptides into nanofibers.[20–22] These SAMDP consist of a central core with alternating hydrophilic and hydrophobic residues that facilitate their self-assembly and surrounding domains that facilitate or regulate assembly. Within water-based solutions, the amphiphilic core facilitates the process of aggregation via hydrophobic packing and hydrogen bonding along the peptide backbone. Meanwhile, the N- and C-terminal domains regulate self-assembly by ion-ion repulsion or steric restrictions. The predominant design of SAMDPs employs ionic residues like lysine, arginine, or glutamate to regulate the process of molecular assembly and hydrogel formation in reaction to variations in pH or the introduction of multivalent ions (**Figure 4.1**).[23]

Hence in the present scenario, we have designed nanoscaled peptide based biomaterials at the molecular level by bottom-up self-assembly, wherein one molecule is synthesized and one unit is self-assembled consecutively. SAMDP have meticulously engineered peptides capable of undergoing systematic self-assembly into persistent secondary structures (α-helix, β-sheet, or random coil), therefore generating diverse aggregation states including fibrils, fibril networks, membranes, and gels. We have incorporated two neurogenic peptides to the SAMDP to enhance the neurogenesis at the injured site and help in tissue regeneration. The hydrogel-forming nature of the composite was first characterized by rheology and vial inversion assay. The secondary structure of the designer SAMDP hydrogel was investigated using circular dichroism Fourier transform infrared spectroscopy.

Then, the biocompatibility of the composite was checked in various cell lines including hMSCs, C2C12 and WI-38. Further, an investigation was conducted to assess the survival, orientation and differentiation of hMSCs within the bioactive nanofiber hydrogel in order to test our research hypothesis, while its contribution for nerve repair was assessed *in vivo* by repairing a critically injured crushed rat nerve defect. Moreover, the effects of peptide composite conduit on nerve regeneration were investigated through behavioural and histological analysis. The results of our

study indicate that the peptide nanofibers show significant potential for clinical use in the remediation of peripheral nerve damage.

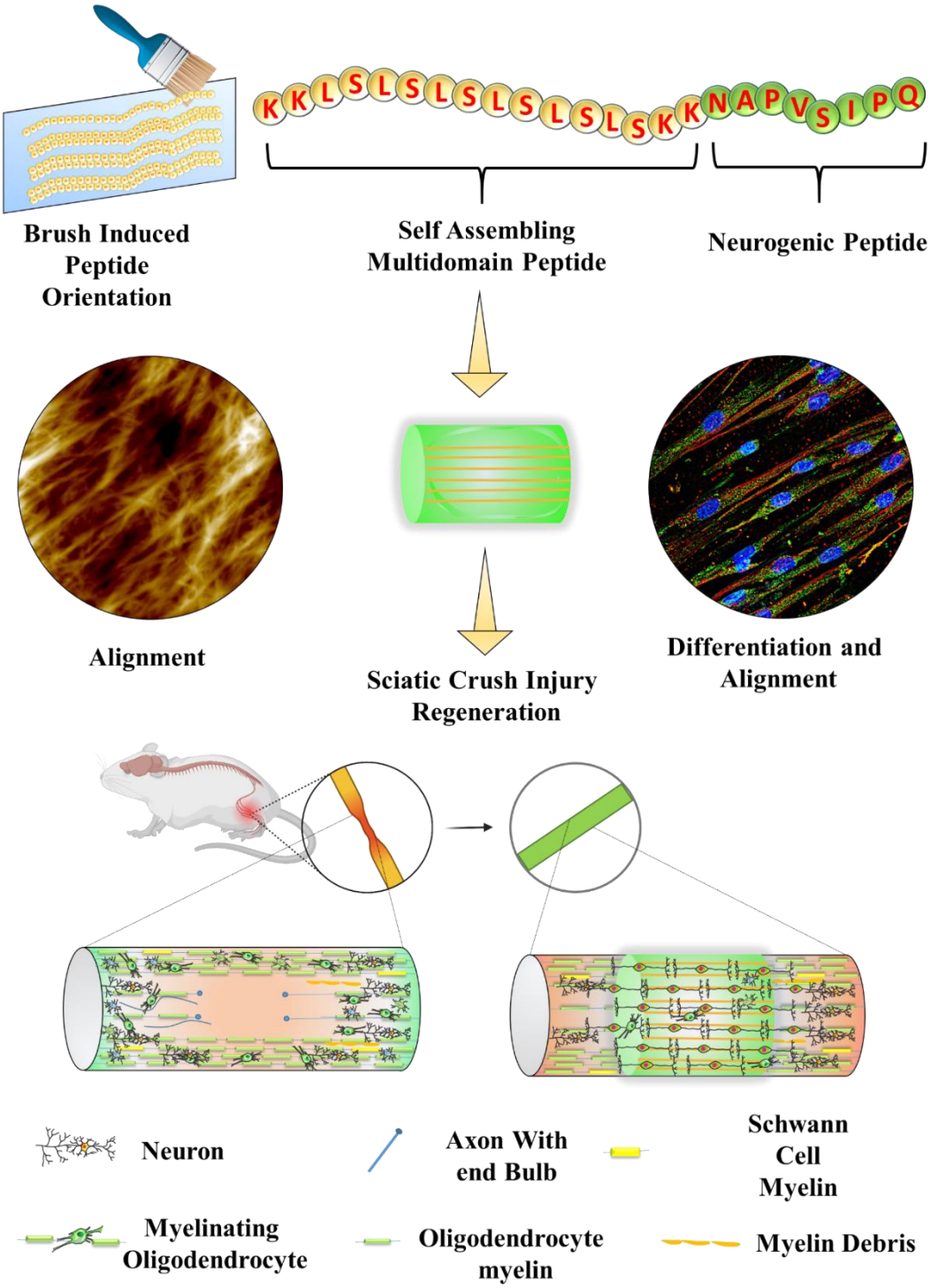


Figure 4.2 Schematic illustration of the mechanism of action of peptide hydrogel for the treatment of SNI.

4.3 MATERIALS AND METHODS

Merck was the source of the following chemicals: Fmoc-Rink Amide AM resin (8.55004.0025), Fmoc-amino acids, HBTU (12804), 5(6)-Carboxyfluorescein (FAM) (MFCD00151081), Phenol, Dichloromethane (DCM)(I10006), 1,2-Ethanedithiol (EDT) (02390), Hydrogen Peroxide (30% solution), and N, N dimethylformamide (DMF)(270547). Methanol, dimethyl sulfoxide (DMSO), pipyridine (011629), diisopropylethylamine (DIPEA) (0104261), diethyl ether, and trifluoroacetic acid (TFA) (012049) were acquired from Spectrochem. The Rink amide AM resin and Fmoc-protected amino acids were acquired from Novabiochem (Germany).

3-(4,5-dimethylthiazol-2-yl)-2,5-diphenyl tetrazolium bromide (MTT) was obtained from Sigma (M2128). FBS was obtained from Invitrogen (2023-01-30), Antimycotic antibiotic solution from Himedia (A002), Penicillin Streptomycin solution from Invitrogen (15140-122), Trypsin EDTA Solution from Sigma (T4174), Bovine Serum Albumin (BSA) from SRL (83803), PVDF Membrane from Millipore, Immobilon Western HRP Substrate from Millipore (WBLU F0500), Anti-Rabbit IgG HRP linked (CST-7074, Dilution 1: 10k), and HRP conjugated secondary Antibody (Anti-Mouse IgG HRP linked, CST 7076, Dilution 1: 5k). Rabbit monoclonal antibody to glyceraldehyde-3-phosphate dehydrogenase (GAPDH) from Cell Signalling Technology (CST), catalogue number 2118. The Goat Anti-Rabbit IgG HandL (Cy3.5 ®) preadsorbed (Abcam, ab6941), Goat anti-mouse IgG H and L Alexa Fluor® 488 (Thermo, A11029, Dilution 1:400), and Hoecsht 33258 (ab228550, Abcam) are the specific antibodies used in this experiment.

4.3.1 Multidomain Nanofiber Peptide Synthesis: The multidomain peptide with the sequence KKLSLSLSLSLSLSKKNAPVSIPQ and KKLSLSLSLSLSLSKKNAVSIQ was synthesised using Rink Amide AM resin in a solid-phase peptide synthesiser (CEM Liberty1, USA). HBTU (5 eq.) and DIPEA (10 eq.) were utilised as coupling reagents, and Fmoc functionality was deprotected using a 20% piperidine solution in DMF (v/v). The peptide was extracted from the resin using a cocktail of TFA, water, EDT, and phenol in the ratio 94:2:2:2 (v/v/v/v) at room temperature for 4 hours, and the peptide was precipitated with cold diethyl ether. SLNAP was lyophilised and purified using reverse phase HPLC (Shimadzu LC-20AP with SPD 20A UV-VIS detector), followed by ESI mass spectrometry analysis (Agilent 6530).[28]

4.3.2 Peptide Hydrogel Preparation for *in vitro* and *in vivo* Assays: The hydrogel is prepared with a peptide concentration of 0.8% (wt/v) and a pH of 7.4. The gel was formed by dissolving 8 mg of all lyophilized peptides in a 298 mM sucrose solution using gentle sonication at 37°C. Further, 1X HBSS was added to the peptide solution following which the solution was left undisturbed for 15 minutes at room temperature. Further, an vial inversion test was conducted on the vial, which conclusively verified the presence of gel formation. The hydrogel underwent sterilisation before to its usage in both in *vitro* and *in vivo* assays by exposing it to UV radiation in a chamber for 2 hours.[14]

4.3.3 Characterization of Peptide Hydrogel: The secondary structure of the peptide hydrogel was determined using Fourier Transform Infrared Spectroscopy (FTIR) and Circular Dichroism (CD). The Vertex 70 Spectrometer (Bruker) was used to detect the presence of amide I and amide II interactions in the peptide. A volume of 50 µL of hydrogel was utilised to get transmittance scans following background correction. A peptide solution with a concentration of 25 µM was prepared using water and PBS. Further, the solution was incubated for a period of 3 days prior to the experiment. [17] CD spectra were obtained using a Jasco J-815 spectropolarimeter, covering a wavelength range of 190 to 250 nm with a step size of 1.0 nm. The nanofibrous morphology of the peptide hydrogel was determined using Atomic Force Microscopy and Field Emission Scanning Electron Microscopy (FE-SEM). For AFM investigation, a 0.1 wt% solution of peptide gel was applied onto a mica sheet. The gel was then dried overnight in a desiccator and subsequently imaged using an XE 70 microscope from Park System. For the FE-SEM analysis a 0.8 wt% SLNAP hydrogel, which was diluted by half and then applied onto a silicon wafer. The hydrogel was subsequently dried under a vacuum. The sample was subjected to sputter coating for 120 seconds at 20 mA, resulting in the observation of a purple plasma bloom. The sample was then scanned using the Apreo 2S Thermo-Fischer Scanning Electron Microscopy.[29–31]

4.3.4 Rheology Study of Peptide Hydrogel: In order to examine the mechanical characteristics of the hydrogel, an initial dynamic frequency sweep experiment was conducted. In summary, different wt% of hydrogels were prepared. The experiment was conducted using an Anton Par MCR102 rheometer equipped with a cone-plate geometry, with a diameter of 40 mm and an angle of 4°. The thixotropic assessment involved using a 2 wt % sample of hydrogel. The experiment was conducted using a 40 mm parallel-plate geometry setup. The strain was abruptly changed from 0.1 to 50% in three cycles, with each cycle lasting 800 ns.[31]

4.3.5 Determination of Cytotoxicity of Different Peptide Hydrogels: The cytotoxicity of the various hydrogels was assessed *in vitro* using the MTT assay, as previously described. hMSCs were cultured in a 96-well plate with a cell density of 2 x 10^5 cells per well and allowed to grow for a duration of 24 hours. Subsequent cells were exposed to different wt% of peptide hydrogels (ranging from 7.8 µg / mL to 1 mg / mL) and were then allowed to grow for an additional 24 hours. Subsequently, MTT was added and the plate was left for an additional 3-4 hrs and the absorbance of the formazon salt formed was measured at 570 nm using a thermal variolux scan microplate reader.[28]

4.3.6 Hydrogel Coated Surface Preparation: In order to create a nanofibrous surface for neuronal differentiation, hydrogel consisting of 0.8 wt% of different hydrogel was coated onto a 35 mm culture dish. It was then allowed to solidify overnight at a temperature of 37 °C. After a period of 12 hours, the surplus hydrogel was removed and the culture dish was delicately washed with filtered PBS two times. In the control group we utilised Tissue Culture Plates (TCPs) in their original state, while for the positive control, the primary E18 culture group employed TCPs that were coated with poly-D-lysine (PDL) according to our previously reported protocol. [32]

4.3.7 *In Vitro* Cytotoxicity Analysis: Initially, human mesenchymal stem cells (hMSCs) were cultured in a 35 mm culture dish at a density of 2 x 10^5 cells/mL and allowed to grow for 24 hours. Further cells were subjected to treatment with different peptide hydrogels. Following treatment, cells were allowed to grow for an additional 24 hours and then stained with calcein-AM (3 μM) and PI (3 μM) in phenol red-free colourless DMEM medium for 10 minutes at 37 °C in the dark in CO_2 incubator. Subsequently, the medium was removed and the cells were rinsed with filtered PBS. The fluorescence images were acquired using a fluorescent microscope (OLYMPUS IX83), with red fluorescence indicating deceased cells and green fluorescence indicating living cells. In addition, the images were quantified using the Image J software.[14]

4.3.8 Scratch Wound Healing Assay with Different Peptide Hydrogels: A scratch assay was conducted to examine the effect of peptide hydrogel on the migration of hMSCs. In summary, the cells were grown in expansion media containing 10% FBS in a 6-well plate until they reached 80% confluence. Subsequently, the cell monolayer in the centre of the plate was gently scraped twice using a new 200 μL pipette in a straight line, resulting in the creation of a scratch. The cellular debris was washed with PBS and the cells were allowed to grow in the treatment medium, consisting of 1% foetal bovine serum (FBS) and 1% wt% of different hydrogel. Images were captured at certain time intervals (0 h, 12 h, and 24 h) using a Dewinter VICTORY microscope that was fitted with a SONY CCD CAMERA.[33]

4.3.9 Brush-Induced Orientation and Transdifferentiation of hMSCs: Microscopic glass slides were cut into 1 x 6 cm^2 rectangular substrates using a sharp diamond pen. Before usage, the glass slides were cleaned by soaking them in 10 mM SDS and 0.1 M HCl at 70 °C for 10 min. Following that they were thoroughly rinsed with deionized water. The substrates were then plasma etched for 2.5 min with air using Harrick PDC-002-HP at a high RF level to remove particles and make the surface negatively charged and hydrophilic before peptide coating. The brushing method was used to get oriented peptide hydrogel substrates. The hydrogel functionalized substrate was supported horizontally and brushed with a nylon paintbrush with stiff bristles always in the same direction. To optimise the buildup of orientation, hydrogel was manually brushed with a nylon paintbrush tilted at 45° to the substrate and allowed left to dry for 10 min, followed by UV steralization and drying with filtered compressed air at 2.5 bar in a vertical direction along the brushing direction.[34]

For the transdifferentiation the hMSCs were cultured on the oriented hydrogel substrate. Briefly, after reaching 70% confluence, cells were plated over the oriented hydrogel surface at a density of 3 x 10^4 cells/cm^2 and they were then maintained in 1% FBS neurobasal media for up to 7 days. After 7 days, cells were immunocytochemically analysed. For double ICC, cells were fixed in 4% formaldehyde at 37 °C for 1h, rinsed with filtered PBS, and permeabilized with 0.1% Trition X-100 for 30 min with 1% BSA for blocking after 7 days. Two more washes with filtered PBS followed overnight incubation with primary antibodies (Tuj1 CST 2146, GFAP Abcam ab7260) at 4 °C. The cells were rinsed twice with PBS before incubating with Goat Anti-Rabbit IgG (H + L) FITC conjugate (Millipore 12-507) secondary antibodies. Nuclear staining with DAPI was done for 30 minutes to see cell nuclei.[35]

4.3.10 Primary Cortical Neuronal Culture: Primary cortical neurons were cultured according to our previously reported methods. Briefly, pregnant female rats between E14 and E18 were chosen for the primary cortical neurons, following the previously published method. In summary, the control group involved culturing cortical neurons in a culture dish coated with poly-D-lysine at a density of 1 x 10^5 cells/mL. On the other hand, for the hydrogel treatment, neurons were cultured on culture dishes coated with the different hydrogels. The culture medium used for the hydrogel treatment included neurobasal media supplemented with 2% B27, 200 mM GlutaMax, 1% pen-strap, and 1% FBS. Additionally, the cells after the treatment were utilised for ICC.[32,36]

4.3.11 Injectability Nature of the Peptide Hydrogel: A syringe is used to determine the injectability of gel, which is an extremely important dimension to consider when applying gel in vivo. After being transformed into a sol condition, the gel is extracted from the glass vial using a syringe and then placed back into the vial.

4.3.12 Animals: The Ethics Committee of the Institute approved all experimental methods employed in this study. Forty male Wistar rats were randomly divided into four groups, with ten rats in each group. The four experimental groups were as follows: (i) Control group, (ii) Crush Injury, (iii) SLANP, (iv) SLNAV, (v) SLOP5, and (vi) Matrigel. Matrigel was utilised as a positive control. The rats were kept in groups of four in cages inside a controlled environment. This environment had a consistent 12-hour cycle of light and darkness, a temperature of 24 ± 1 °C, a relative humidity of 40–60%, and the rats had unrestricted access to food and water.[37]

4.3.13 Generation of Sciatic Nerve Crush Injury Model: In brief, Sciatic nerve crush injury was performed as previously described. Around 8-10-week-old Male Sprague-Dawley rats (average weight 250 g) were acquired from JNVU. Rats were anaesthetized first with Intraperitoneally administer of 2% xylazine hydrochloride and 10% ketamine hydrochloride at a dose of 20 mg/kg and 80 mg/kg, respectively, hair on the left and right femur was trimmed, and the area was cleansed and sterilized with betadine and 70% isopropyl alcohol swabs. The sciatic nerve was revealed by making a subcutaneous incision at the thigh and gently separating the intermuscular area.[38] The nerve was crushed with fine forceps for 20s twice. When the nerve was crushed, animals were randomly divided into five groups (Injury, SL, SLNAP, SLNAV and Matrigel), around 10 µL of the different peptide hydrogel or matrigel was injected into the damage site with a glass needle and an auto-nanoliter Stoelting Quintessential Stereotaxic Injector (QSI™). The injury group received only saline as a treatment. For investigation of sciatic nerve cross-sections, the injury location was identified with a suture 5 mm distal from the crush injury. The skin was sutured, and animals were allowed to recover and were observed routinely during the course of the behaviour trial. All animal experiments were performed after receiving approval from the animal ethics committee.

4.3.14 Beam Walking Motor Coordination Assay: The "beam-walking" assay was conducted according to the previously reported protocol with some modifications, using a self-made experimental arrangement. In brief, we used a 17 mm circular plastic beam, an 11 mm circular plastic beam, and a 5 mm square wooden beam. During the training period, the rats underwent walking training on the beams for three consecutive days, with four trials each day, in order to cross the beam and enter the home cage. After achieving a consistent level of performance, the mice were subjected to three successive trials on the 17 mm and 11 mm circular plastic beams, as well as the 5 mm square wooden beam. The order of testing started with the widest beam and progressed to the narrowest beam. The time it took to cross the central 80 cm of each beam and the frequency of hind-paw slippage were documented for each attempt. The average scores for each beam at a specific time point were utilised in the analysis.[39]

4.3.15 Calculation of Sciatic Nerve Function Index (SFI): The sciatic function index (SFI) is a widely used method for evaluating functional abilities. It employs mathematical techniques to compare the characteristics of control normal footprints with those of experimental (treatment and injury) footprints. The text provides information about the restoration of motor-sensory connections and brain integration associated with walking function, which is facilitated by the sciatic nerve.

The assessment of nerve function recovery following injury was conducted by a walking track and footprint analysis. At designated time intervals, the hind paws of the animals were marked with a non-toxic dye and allowed to walk on a 5 × 32-inch walking track covered with white paper.[40]

Applying the Bain equation, we obtain: SFI = −38.3 (PLF) + 109.5 (TSF) + 13.3 (ITF) − 8.8. Further data obtained was plotted using a graphpad prism.

Print length factor (PLF): [experimental print length (EPL) − normal print length (NPL)]/NPL. Toe spread factor (TSF): [experimental toe spread (ETS) − normal toe spread (NTS)]/NTS. Intermediary toe spread factor (ITF): [experimental intermediary toe spread (EIT) − normal intermediary toe spread (NIT)]/NIT.

4.3.16 Histology and Staining: After perfusion, tissue samples were collected and fixed overnight with 4% PFA and processed further for cryosectioning using a sucrose gradient solution. Nerves were embedded in OCT and frozen before cutting them into 10 μm sections and were further processed for H & E (haematoxylin and eosin), following a previously reported protocol.

4.3.17 Haematoxylin and Eosin of Gastromeniscus Muscles: After perfusion fixation, tissue samples were collected and utilised for H & E (haematoxylin and eosin) staining, following a previously established protocol. To summarise muscle tissue slices measuring 5 μm underwent a cleaning process using xylene, followed by rehydration using a series of ethanol washes. Afterwards, the slices were stained with hematoxylin and eosin for a period of 2 minutes. Afterwards, the samples were affixed using DPX mounting media. Subsequently, the slices were cleansed, dehydrated utilising a gradual ethanol gradient, purified with xylene, and ultimately affixed in DPX.[41]

4.3.18 Statistical Analysis: All data reported as the mean with standard deviation (SD) were derived from a minimum of three or four distinct studies. A one-way analysis of variance (ANOVA) was conducted to compare the mean values of more than two distinct groups, using Prism software (GraphPad Software Inc., Version 3.0, California, United States) for the analysis. A statistic was deemed statistically significant if its p-value was below 0.05. Certain elements of the figures were created with Biorender.

4.4 RESULTS AND DISCUSSION

4.4.1 Biomimetic SAMDPs spontaneously form nanofibrous scaffolds through self-assembly: A set of SAMDPs was synthesized to facilitate nerve regeneration. This was achieved by integrating small peptide mimics NAP (NAPVSIPQ)[17] and NAV (NAVSIQ)[24] which share a structural similarity with the active component of ADNF-9[25] that promotes neurite outgrowth into a $K_2(SL)_6K_2$ motif, as shown in Table 1 (**Figure 4.2 and 4.3**). The selection of alternate serine and leucine is based on the vasopressin receptors (V1VP) expressed in hippocampus neurons.[25,26] These receptors have been shown to provide neuroprotection against glutamate-induced neuronal cell death and also exhibit anti-apoptotic properties. As previously mentioned, SAMDPs like K_2 have a tendency to spontaneously arrange themselves into antiparallel β-sheet structures.[27] These structures can then form injectable hydrogels when ultra-sonicated. Images obtained using atomic force microscopy (AFM) showed that the polymeric $K_2(SL)_6K_2$ hydrogel network has fibrous characteristics (**Figure 4.4A**).

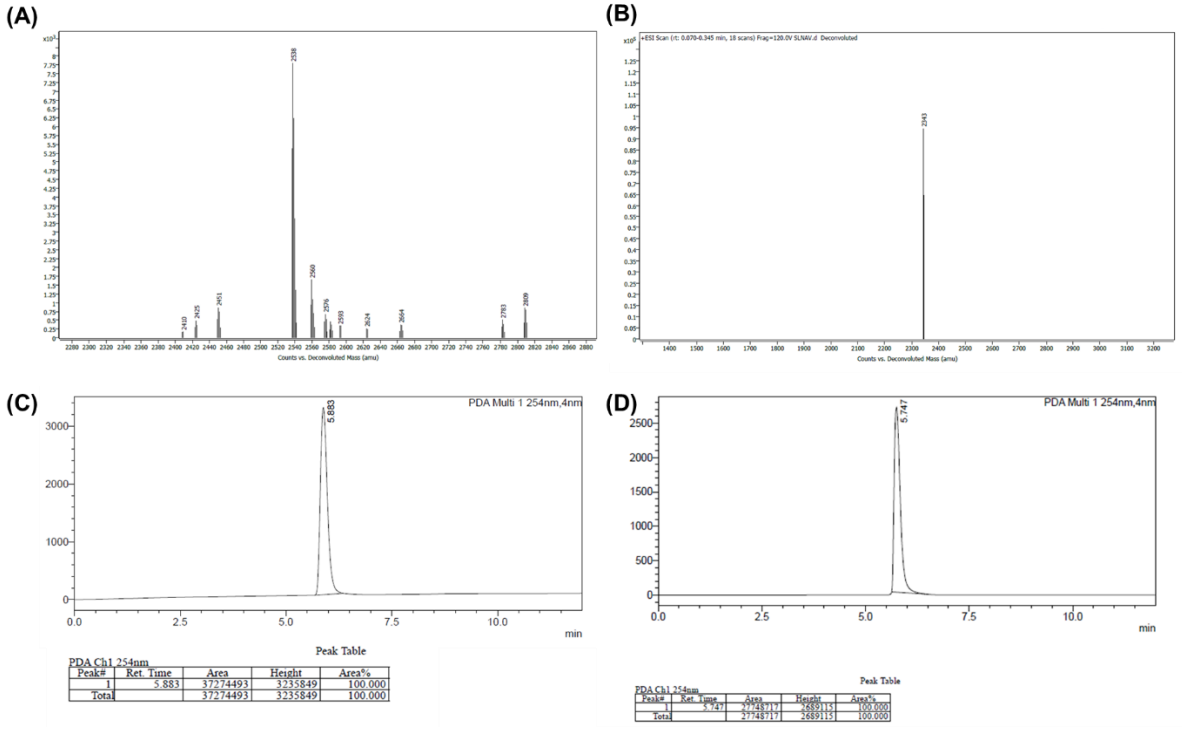


Figure 4.3 (A) ESI Mass spectra of $K_2(SL)_6K_2$NAP peptide, (B) ESI Mass spectra of $K_2(SL)_6K_2$NAV peptide, (C) HPLC of $K_2(SL)_6K_2$NAP peptide, (D) HPLC of $K_2(SL)_6K_2$NAV peptide

Following the incorporation of the neuroprotective mimetic peptide motifs, we analyzed the secondary structure, assembly, and rheological properties of the resultant materials. The addition of 6-8 residues was found to have minimal impact on the antiparallel β-sheet structure, as demonstrated by Fourier-transform infrared spectroscopy (FTIR) and circular dichroism (CD) analysis (**Figure 4.4 B, C**). The resultant peptides exhibited a minimum absorption at approximately 216 nm and a maximum absorption at approximately 198 nm in circular dichroism (CD) spectroscopy. Additionally, the peptides displayed infrared (IR) peaks at 1695 cm−1 and near 1620 cm−1, which are collectively indicative of this particular conformation (**Figure 4.4 A-L**).

FT-IR spectroscopy established the secondary structure of both peptides, as shown in **Figure 4.4 (B)** correspondingly. An essential characteristic for evaluating the structure of a protein is the Amide I vibrational band about 1600-1700 cm-1. The prominent peaks observed at 1615 cm-1 and 1635 cm-1 correspond to the intermolecular and intramolecular beta-sheet structures, respectively.

4.4.2 A Peptide Hydrogel That Assembles Itself and Its Mechanical and Physical Properties: Based on our previous observations we were intrigued to investigate the tendency of self-assembly and the ability to produce hydrogels in all the peptide amphiphiles that were designed. Based on our experimental findings (vial inversion assay), it has been seen that all the peptides that were synthesized have the ability to form hydrogels in PBS. This self-assembly process is supported by the peptides themselves. However, it is important to note that the critical gelation concentration of each peptide varies.

Initially, we used a concentration of 1 wt% of $K_2(SL)_6K_2$. However, even after repeated heating and cooling and incubating for 12 hours, this concentration did not result in the formation of a self-supporting hydrogel structure. By increasing the concentration of $K_2(SL)_6K_2$ to 2 wt %, we observed the formation of a hydrogel scaffold. This hydrogel scaffold was not able to maintain its gel-like structure after the vial was inverted in an experiment; instead, it remained a cloudy solution. Subsequently, we increased the concentration of $K_2(SL)_6K_2$ to 3 wt %. Interestingly, the $K_2(SL)_6K_2$ at 3 wt % this hydrogel scaffold was able to maintain its gel-like structure even after the vial was inverted in an experiment. Based on our findings, we have determined that the minimum concentration of $K_2(SL)_6K_2$ required for gelation in the production of a multicomponent coassembled hydrogel matrix is 3 wt %.

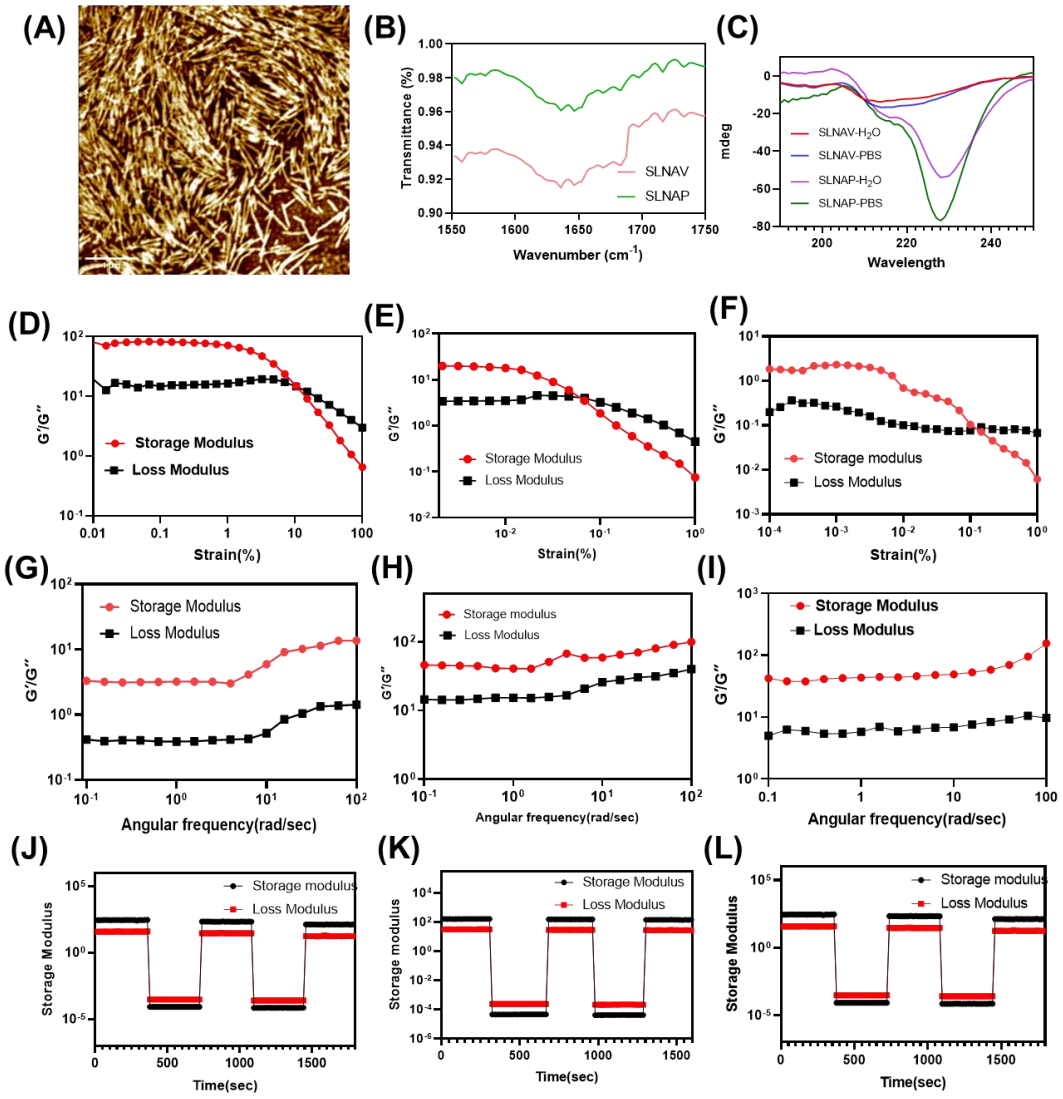


Figure 4.4 AFM characterization of the $K_2(SL)_6K_2$ peptide nanofiber, (B) FT-IR spectroscopy of the $K_2(SL)_6K_2$NAP and $K_2(SL)_6K_2$NAV peptide nanofibers confirming generation of b sheets. (C) CD spectra confirming formation of beta sheet structure, (D), (E), (F) Strain sweep study of $K_2(SL)_6K_2$, $K_2(SL)_6K_2$NAP and $K_2(SL)_6K_2$NAV respectively, (G), (H), (I) Dynamic frequency sweep study of $K_2(SL)_6K_2$, $K_2(SL)_6K_2$NAP and $K_2(SL)_6K_2$NAV respectively. Scale bar corresponds to 1µm.

Interestingly, on the other hand, $K_2(SL)_6K_2$NAP and $K_2(SL)_6K_2$NAV will form hydrogel even at a lower concentration of 0.8 wt %. This study is interesting because it gives proof that even when the weight percentage of $K_2(SL)_6K_2$NAP and $K_2(SL)_6K_2$NAV is decreased, the coassembly of $K_2(SL)_6K_2$NAP and $K_2(SL)_6K_2$NAV can still occur, resulting in the formation of hydrogel-like scaffolds. Further, the AFM analysis was conducted to examine the topography of $K_2(SL)_6K_2$NAP at concentrations of 0.8 wt %. The results revealed the presence of a network of interwoven nano fibrillary structures, as depicted in **Figures 4.5 A, B**.

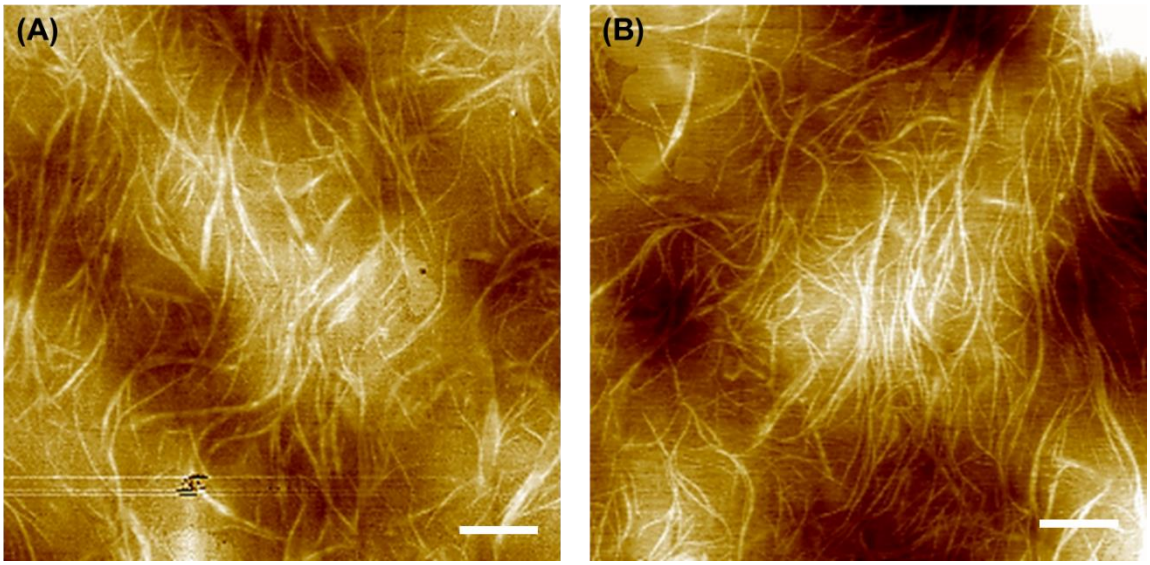


Figure 4.5: AFM images of (A) $K_2(SL)_6K_2$NAP and (B) $K_2(SL)_6K_2$NAP peptide nanofibers. Scale bar corresponds to 1 µm.

In order to assess the mechanical characteristics of the material, we conducted a rheology investigation on our $K_2(SL)_6K_2$NAP and $K_2(SL)_6K_2$NAV hydrogel. A material is considered to have a "gel" like character when the storage modulus (G') is significantly larger than the loss modulus (G") in the frequency range of 0.1-100 Hz.

Further, to check the mechanical property of the hydrogel, we performed the rheology and based on the frequency sweep experiment depicted in **Figure 4.4 D-I**, we observed a significant difference between the storage and loss modulus for all hydrogels. If the storage modulus value is higher than the loss modulus, it indicates that all four components are present in their hydrogel-like condition. A strain sweep study (**Figure 4.4 D-F**), is conducted to observe the linear viscoelastic region (LVR) of the material. The storage and loss moduli in LVR do not vary with the applied strain. Subsequently, we conducted a time-dependent step-strain experiment at room temperature using our 0.8 wt% hydrogel to assess its thixotropic characteristics. The application of shear thinning and reassembly kinetics at the wounded region is highly important parameter. In this experiment, we initially subjected the sample to a consistent and low strain of 0.1% for the first 120 seconds. Subsequently, we abruptly increased the strain to 50% for the next 200 seconds. Finally, we decreased the strain back to a lower value of 0.1% to assess the hydrogel's ability to restore its original state (**Figure 4.4 J-L**).

4.4.3 Biocompatibility of the Peptide Hydrogel: The biocompatible nature of the peptide hydrogel was evaluated with three different cell lines stem cells (hMSCs), fibroblasts (WI-38) and muscles (C2C12). For that purpose, the cells were grown on the appropriate media, and then cells were treated with different concentrations of three different peptide hydrogels. As shown in **Figure 4.6 A-I,** the MTT results show that the peptide hydrogel was highly biocompatible with the delegate cell lines like stem cells as evident with around 70% cell viability even at a higher concentration of 1 wt% (Table S1-S3).

Further, we have validated the results with the phalloidin staining of hMSCs and C2C12 cells. As shown in **Figure 4.7 A-H,** after treating with different peptide hydrogels the cells were healthy and in good shape. Further, live dead imaging using the calcein-AM/PI was done to evaluate the biocompatibility of the hMSCs at different time periods day 3 and day 7 (**Figure 4.8**). The results obtained show totally green live cells, which shows a good biocompatibility of the hydrogel.

4.4.4 Investigation of Alignment Parameters: To perform the alignment of the peptide nanofibers, the brush was used to perform manually oriented hydrogel nanofibers on a glass substrate. However, non-oriented hydrogel was obtained by simply dipping the glass surface in the peptide hydrogel. Further AFM was performed to analyse the fiber arrangement and surface topography of the peptide nanofiber ($K_2(SL)_6K_2NAP$) (**Figure 4.9 A, B**). In addition to visual examination, the alignment of fibers was assessed from the AFM images using two distinct methods: spectral determination of orientation and quantitative analysis of surface roughness plots. The presence of aligned fibers was identified in the AFM images. This discovery was further supported by the orientation plots of the respective surface values illustrated in **Figure 4.9 E**.

Figure 4.9 C-G presents a specific illustration of the structure-tensor analysis generated by the OrientationJ plugin for Fiji/ImageJ.1. A HSB (hue, saturation, and brightness) cylindrical coordinate color representation has been selected for the purpose of visualizing the results. The HSB components are associated with the magnitudes of the orientation angle (**Figure 4.9 D, E**), coherence (**Figure 4.9 F**), and the input image, respectively. An advantage of the suggested model is its ability to establish a direct correlation between the quantities to be shown and the colour coding schemes. The angle around the central vertical axis in the cylindrical-coordinate colour representation is directly proportional to the hue (**Figure 4.9 G**). The distance along the axis is directly proportional to the brightness, therefore ensuring the preservation of the original structures' visibility. The distance from the axis is directly proportional to saturation: a greater coherence results in a larger saturation of the corresponding colours (**Figure 4.9 E**).

Further, the FE-SEM was performed on $K_2(SL)_6K_2NAP$ peptide nanofibers after alignment with the brush orientation direction, and their alignment parameters (Coherency, Orientation, Color Survey, Vector field) were calculated, which were also consistent with the AFM results (**Figure 4.10 A-F**). The FE-SEM images showed a high degree of alignment in the $K_2(SL)_6K_2NAP$ peptide nanofibers, confirming the accuracy of the alignment process (**Figure 4.10 D**). This alignment is crucial for applications requiring precise orientation of nanofibers, such as in tissue engineering or sensor development.

To confirm the alignment of the peptide nanofibers. We also checked the alignment of the fluorescent peptide nanofiber after conjugating the peptide hydrogel nanofibers ($K_2(SL)_6K_2NAP$ and $K_2(SL)_6K_2NAV$) with the FITC (**Figure 4.10 F-L**). We have calculated all the alignment parameters (Coherency, Orientation, Color Survey, Vector field), and as expected, the peptide nanofibers were aligning in the same direction of the brush orientation. This alignment was crucial for the overall functionality and

performance of the peptide hydrogel, as it allowed for optimal interaction with surrounding cells and tissues. The results of this alignment analysis will be instrumental in further optimizing the design and application of these peptide nanofibers in biomedical applications (**Figure 4.11**).

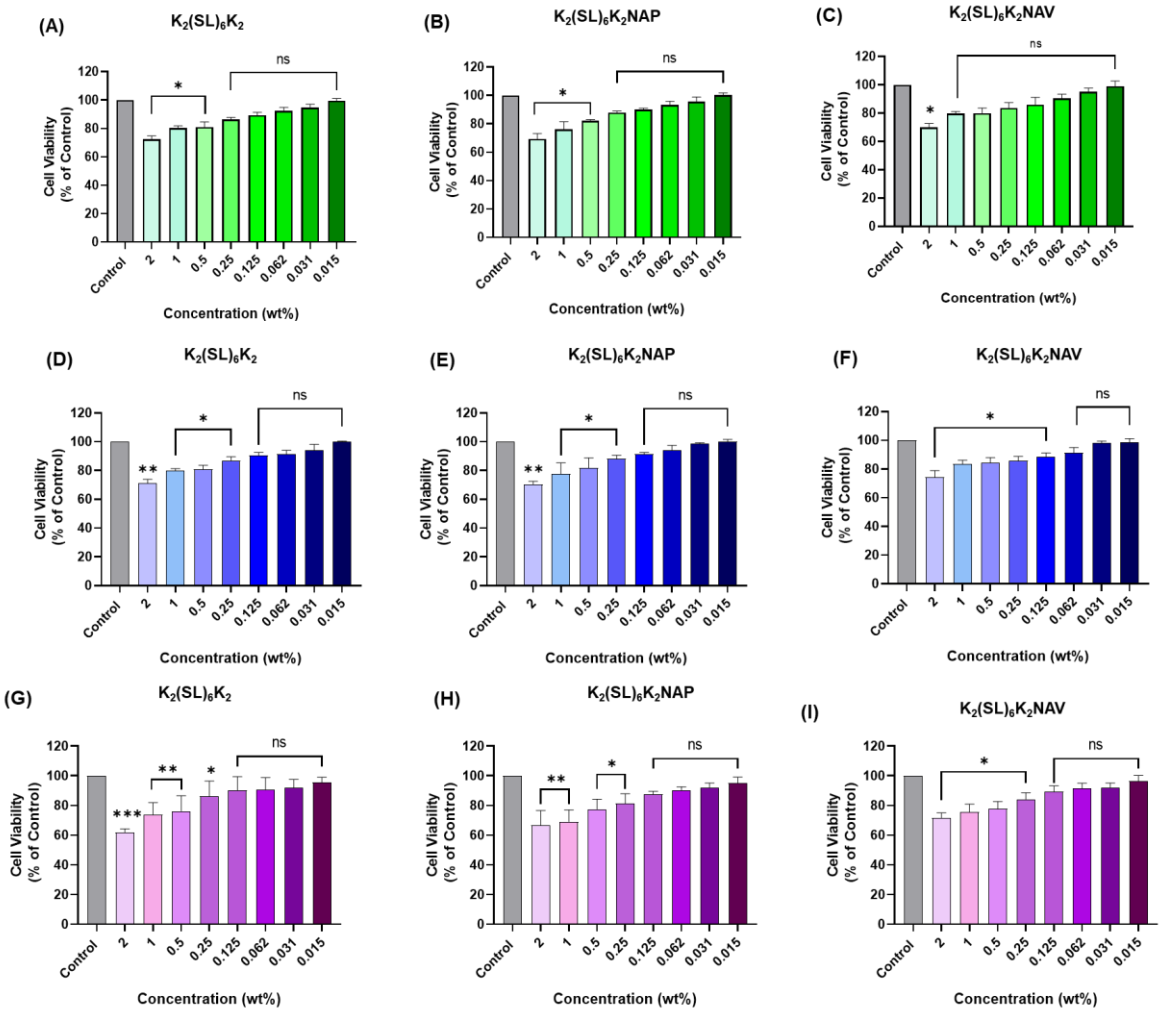


Figure 4.6 Cell viability assay (MTT assay) of hMSCs treated with different wt% of (A) $K_2(SL)_6K_2$, (B) $K_2(SL)_6K_2$NAP and (C) $K_2(SL)_6K_2$NAV hydrogel, Cell viability assay (MTT assay) of WI-38 treated with different wt% of (D) $K_2(SL)_6K_2$, (E) $K_2(SL)_6K_2$NAP and (F) $K_2(SL)_6K_2$NAV hydrogel, Cell viability assay (MTT assay) of C2C12 treated with different wt% of (G) $K_2(SL)_6K_2$, (H) $K_2(SL)_6K_2$NAP and (I) $K_2(SL)_6K_2$NAV hydrogel. Data are represented as the mean ± s.d. from three independent experiments. Significances are marked as *P < 0.05, **P < 0.01, and ***P < 0.001; one-way analysis of variance (ANOVA).

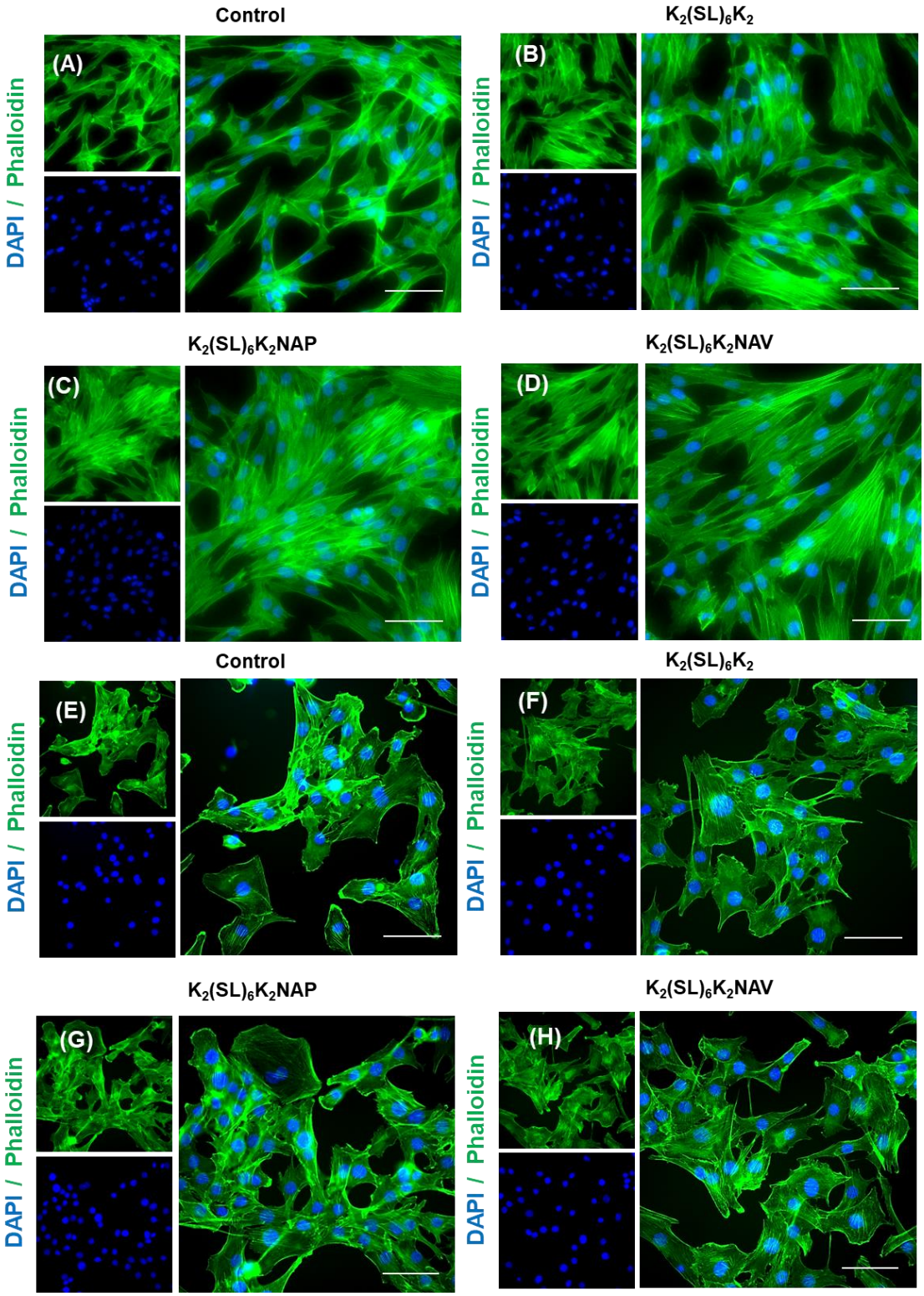


Figure 4.7 Cytoskeleton evaluation of hMSCs cultured on different peptide hydrogels. Fluorescent microscopic images of hMSCs stained with Phalloidin to check the cytoskeleton and counterstained with DAPI after treating with different peptides Control (A), $K_2(SL)_6K_2$ (B), $K_2(SL)_6K_2NAP$ (C) and $K_2(SL)_6K_2NAV$ (D)for 24 h. Cytoskeleton evaluation of C2C12 cultured on different peptide hydrogels. Fluorescent microscopic images of C2C12 stained with Phalloidin to check the cytoskeleton and counterstained with DAPI after treating with different peptides Control (E), $K_2(SL)_6K_2$ (F), $K_2(SL)_6K_2NAP$ (G) and $K_2(SL)_6K_2NAV$ (H)for 24 h. Scale bar corresponds to 50 µm.

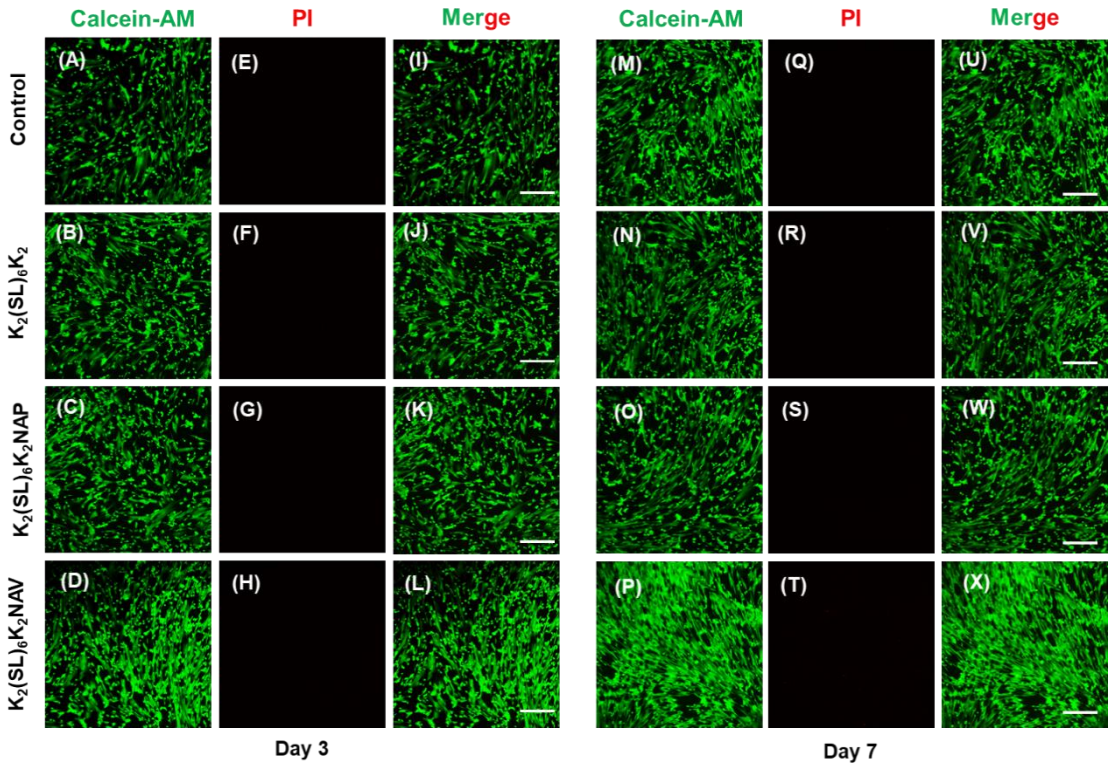


Figure 4.8 Live and Dead assessment of hMSCs. Calcein-AM / PI images of hMSCs under Control (A, E, I), $K_2(SL)_6K_2$ (B, F, J), $K_2(SL)_6K_2NAP$ (C, G, K) and $K_2(SL)_6K_2NAV$ (D, H, L) treatment with different peptide hydrogel at different point of time Day 3 and under Control (M, Q, U), $K_2(SL)_6K_2$ (N, R, V), $K_2(SL)_6K_2NAP$ (O, S, W) and $K_2(SL)_6K_2NAV$ (P, T, X) at Day 7. Scale bar corresponds to 200 µm.

4.4.5 Scratch Wound Healing Assay: A scratch wound healing assay was conducted to assess the ability of the hydrogel to enhance the migration of hMSCs. As depicted in (**Figure 4.12**), it is evident that hydrogel has the capability to augment the migration of stem cells from the surrounding area to the wounded region, hence facilitating tissue remodelling in SNI. Among all the treatment groups the $K_2(SL)_6K_2NAV$ showed the maximum healing with minimum scratch area left after 24 hrs. This suggests that the hydrogel has promise for use in regenerative medicine applications, particularly in facilitating tissue repair and regeneration.

4.4.6 hMSCs Align and Differentiate on the Peptide Nanofibers: Studies have demonstrated that the topographical features of biomaterials play a crucial role in controlling several behaviours of stem cells, including cell adhesion, proliferation, self-renewal, gene expression, morphology, and differentiation. Particularly influenced by the well-defined characteristics of natural extracellular matrices (ECMs) in nerve tissues, aligned nanofibrous scaffolds have been extensively employed as topographical indicators to regulate the activities of stem cells.

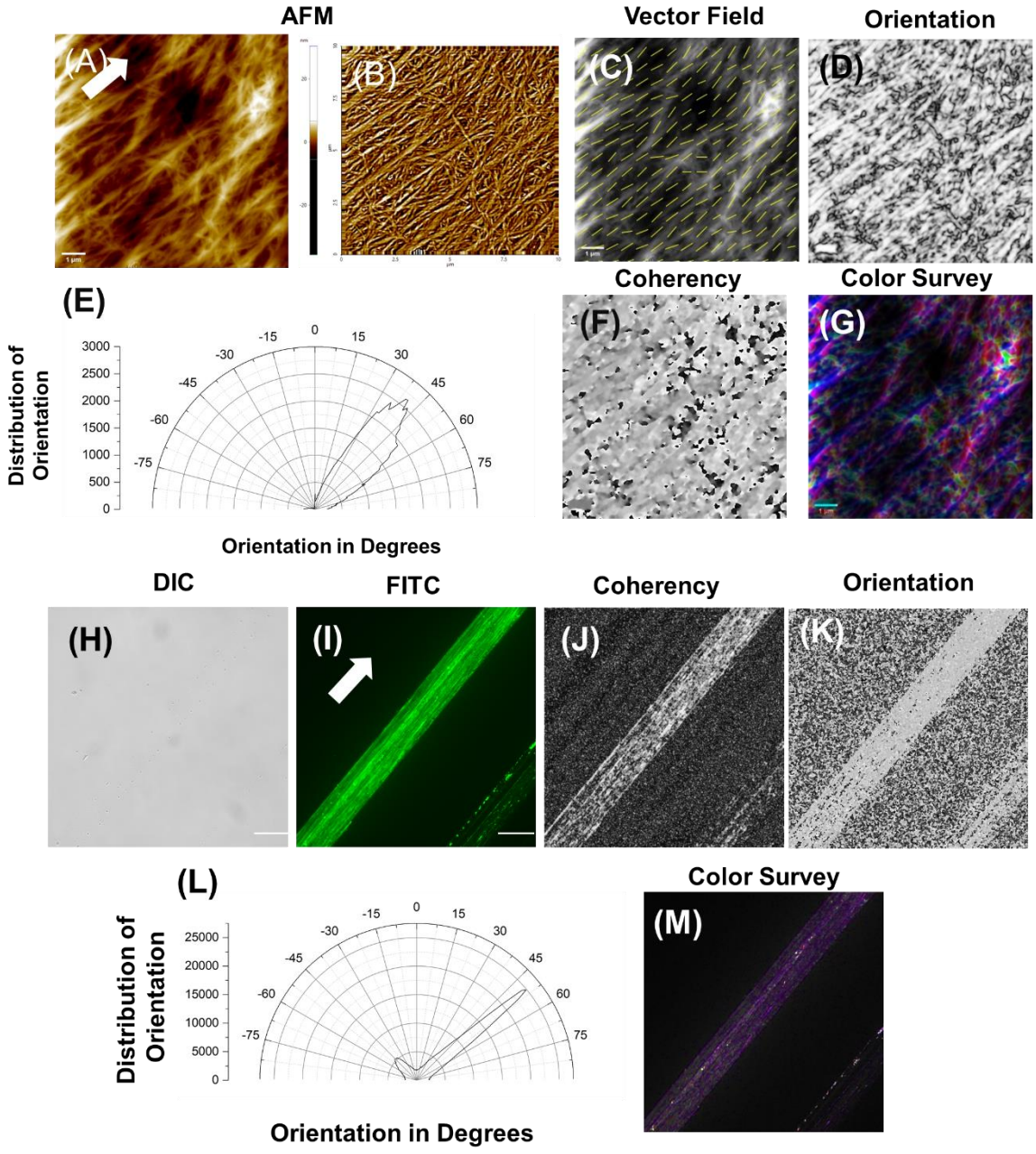


Figure 4.9 (A), (B) AFM images of $K_2(SL)_6K_2$NAP peptide nanofibers (C) Vector field of aligned cells where the orientation is evaluated for every patch of the image based which allows to visualize the orientation of the vector (D) Orientation calculated from the orientation J, (E) Orientation angle derived from orientation J plugin (F) Coherency map: coherency values close to 1.0 are represented in white, coherency values close to 0.0 are represented in black, (G) The color representation reflects the different orientations, (H), (I) DIC and FITC tagged $K_2(SL)_6K_2$NAP, (J) Coherency map: coherency values close to 1.0 are represented in white, coherency values close to 0.0 are represented in black, (K) The color representation reflects the different orientations (L) Orientation angle derived from orientation J plugin (M) The color representation reflects the different orientations. Scale bar corresponds to 1 µm in (A) and 200 µm in (H) and (I) respectively.

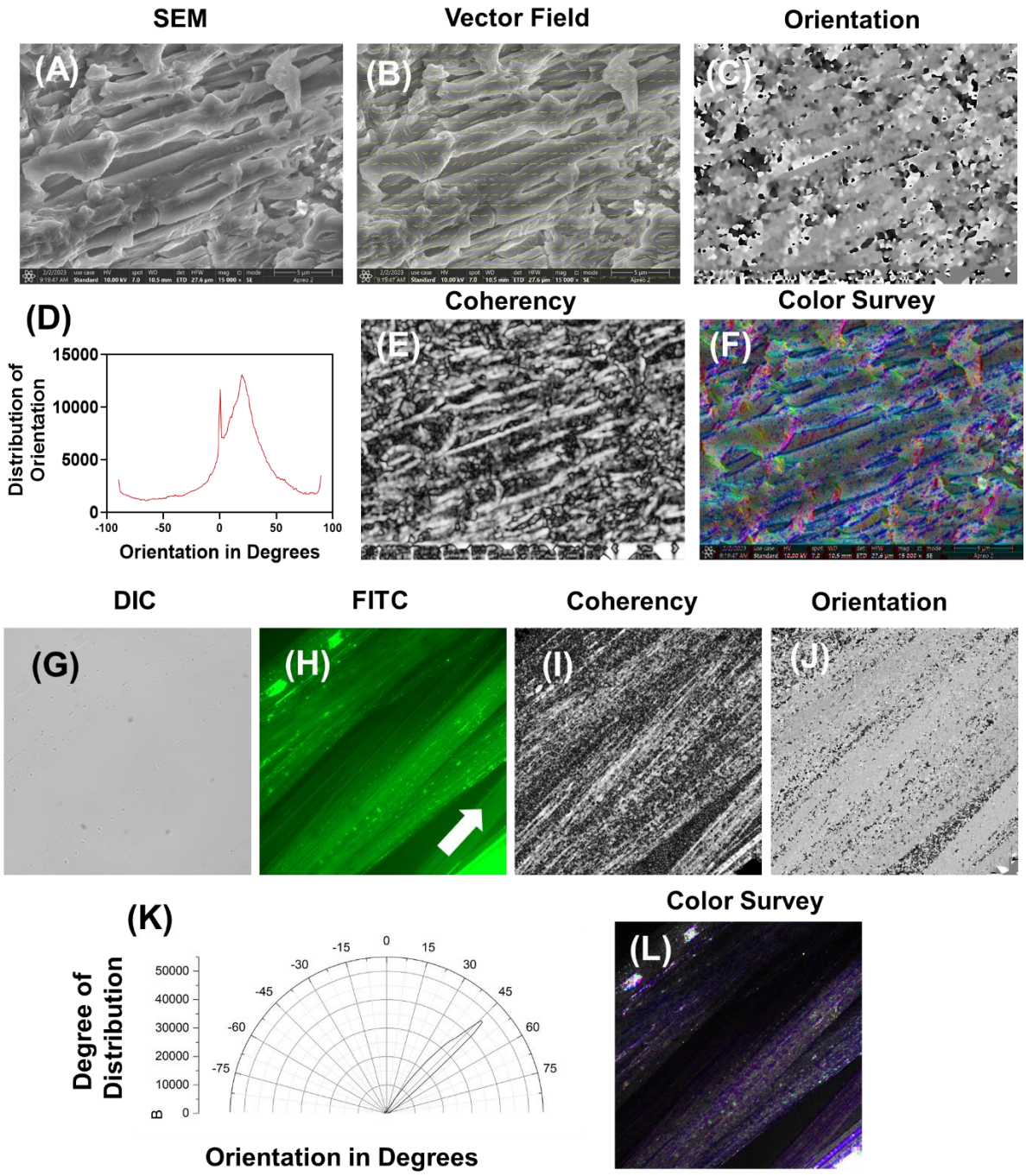


Figure 4.10 (A) SEM of $K_2(SL)_6K_2NAP$ peptide nanofibers, (B) Vector field of aligned cells where the orientation is evaluated for every patch of the image based which allows to visualize the orientation of the vector (C) Orientation calculated from the orientation J, (D) Orientation angle derived from orientation J plugin (E) Coherency map: coherency values close to 1.0 are represented in white, coherency values close to 0.0 are represented in black, (F) The color representation reflects the different orientations. (G), (H) DIC and FITC tagged $K_2(SL)_6K_2NAP$, (I) Coherency map: coherency values close to 1.0 are represented in white, coherency values close to 0.0 are represented in black, (J) The color representation reflects the different orientations (K) Orientation angle derived from orientation J plugin (L) The color representation reflects the different orientations. Scale bar corresponds 200 μm in (G) and (H) respectively.

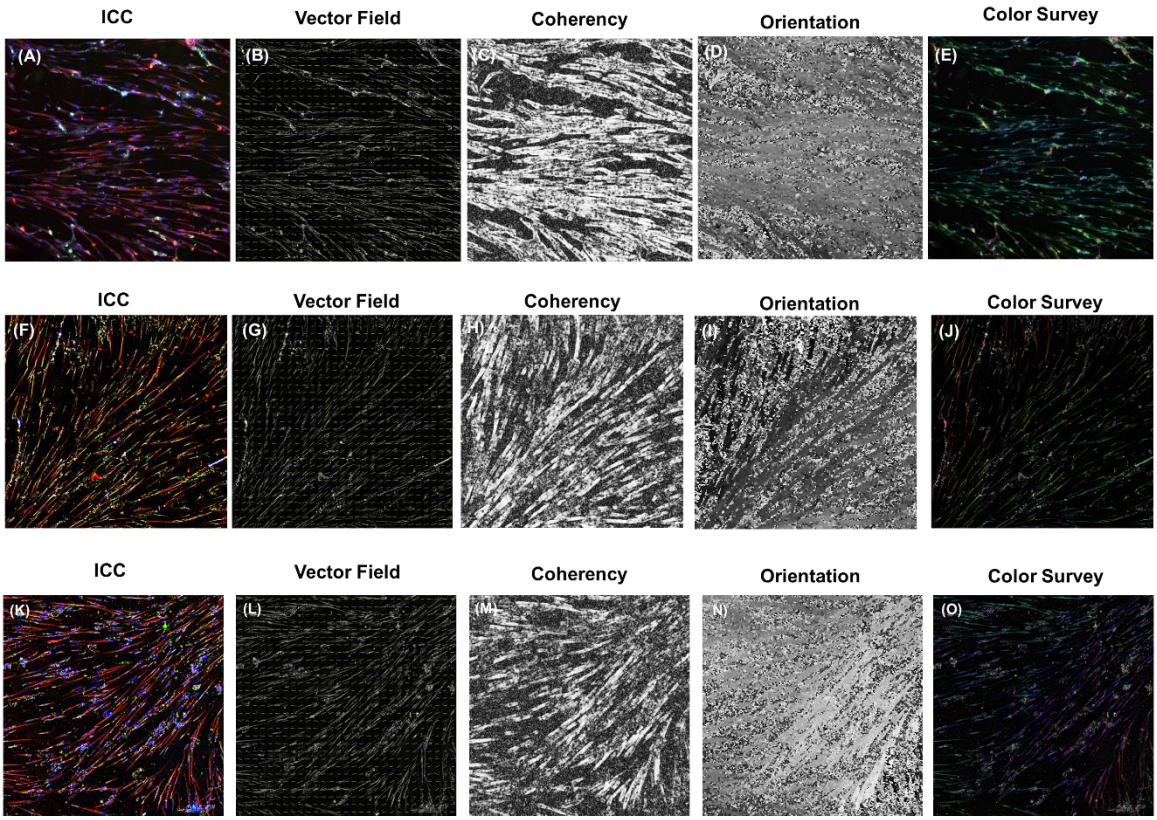


Figure 4.11 Alignment and differentiation of hMSCs derived neurons. (A) Fluorescent images of the hMSCs derived neurons cells with the induction of differentiation for 7 days with $K_2(SL)_6K_2$ conditions. (B) Vector field of aligned cells where the orientation is evaluated for every patch of the image based which allows to visualize the orientation of the vector (C) Coherency map: coherency values close to 1.0 are represented in white, coherency values close to 0.0 are represented in black (D) Orientation calculated from the orientation J (E) The color representation reflects the different orientations. (F) Fluorescent images of the hMSCs derived neurons cells with the induction of differentiation for 7 days with $K_2(SL)_6K_2$ conditions. (G) Vector field of aligned cells where the orientation is evaluated for every patch of the image based which allows to visualize the orientation of the vector (H) Coherency map: coherency values close to 1.0 are represented in white, coherency values close to 0.0 are represented in black (I) Orientation calculated from the orientation J (J) The color representation reflects the different orientations. (K) Fluorescent images of the hMSCs derived neurons cells with the induction of differentiation for 7 days with $K_2(SL)_6K_2$ conditions. (L) Vector field of aligned cells where the orientation is evaluated for every patch of the image based which allows to visualize the orientation of the vector (M) Coherency map: coherency values close to 1.0 are represented in white, coherency values close to 0.0 are represented in black (N) Orientation calculated from the orientation J (O) The color representation reflects the different orientations. Scale bar corresponds to 200 µm.

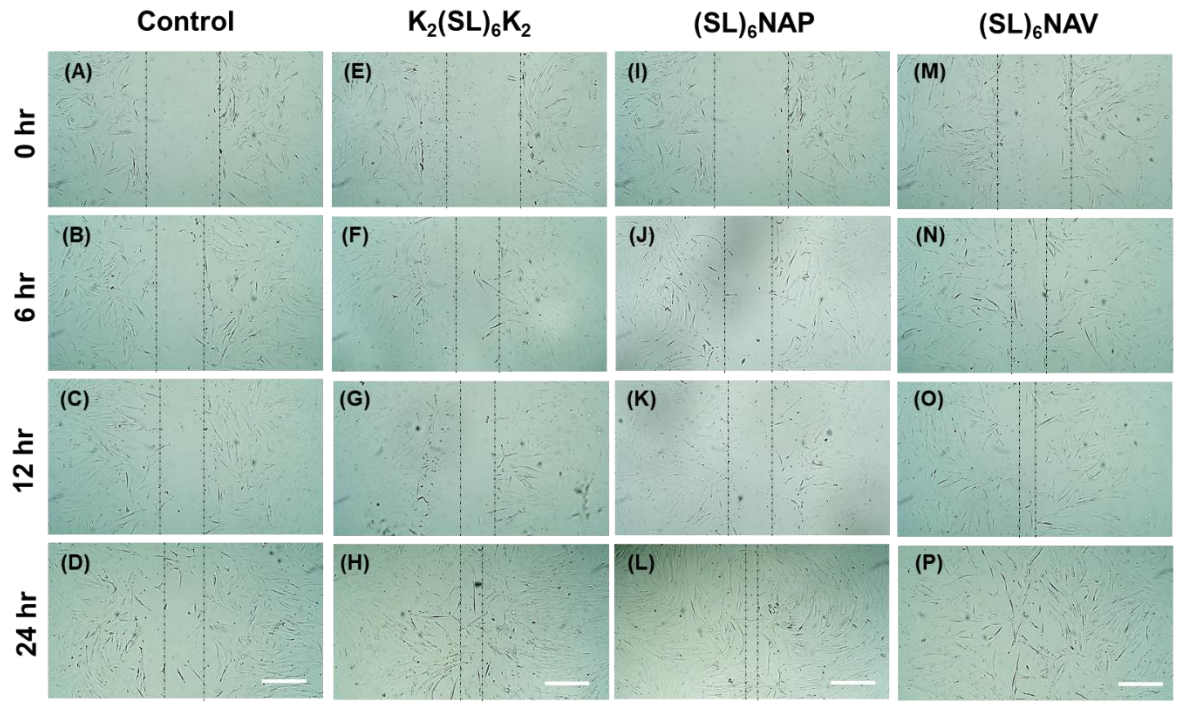


Figure 4.12 Cell scratch assay for the evolution of wound closure at various time points (0-24h): (A-D) wound closure on control TCPs without any external factor, (E-H) wound closure on $K_2(SL)_6K_2$ hydrogel treated TCPs, (I-L) wound closure on $K_2(SL)_6K_2$NAP hydrogel treated TCPs, (M-P) wound closure on $K_2(SL)_6K_2$NAV hydrogel treated TCPs. Scale bar corresponds to 200 µm.

We hypothesised that hMSCs cells would perceive and orient themselves in the direction of nanofibrillar alignment and that a stronger alignment of the scaffold would enhance the guidance of cellular configuration.

The orientation alignment of hMSCs on different peptide nanofibers was determined using immunocytochemistry to label actin filament. hMSCs were cultured on brush-oriented peptide nanofibers and an uncoated glass for 24 hours in a growth medium. This was followed by another 24 hours in a differentiation medium without any further supplements. After incubating, the cells were allowed to differentiate for another 5 days. Confocal microscopic images were taken and were analyzed using orientation J software and as shown in **Figure 4.13.**

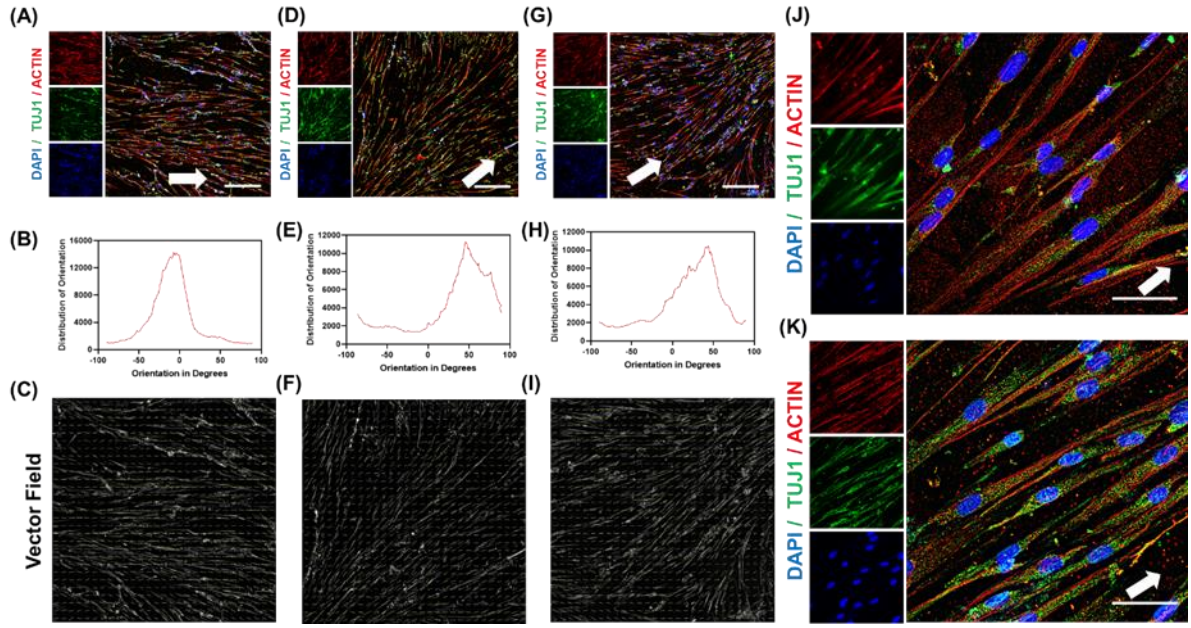


Figure 4.13 Alignment and differentiation of hMSCs derived neurons. Fluorescent images of the hMSCs derived neurons cells with the induction of differentiation for 7 days with different treatment conditions $K_2(SL)_6K_2$ (A), $K_2(SL)_6K_2$NAP (D) and $K_2(SL)_6K_2$NAV (G). The graphs are corresponding histograms of the angular distribution of neurons with different treatment conditions $K_2(SL)_6K_2$ (B), $K_2(SL)_6K_2$NAP (E) and $K_2(SL)_6K_2$NAV (H). Illustrations of the corresponding vector field of the angular distribution of neurons with different treatment conditions $K_2(SL)_6K_2$ (C), $K_2(SL)_6K_2$NAP (F) and $K_2(SL)_6K_2$NAV (I) Fluorescent images of the hMSCs derived neurons cells at higher magnification of 60x. Cells were stained for anti-Tuj1 (green), anti-actin (red) and DAPI (blue). Scale bars indicate 100 µm in A, D, G and 20 µm in J and K.

On the brush oriented nanofibers, the immunostaining showed that the cell aligned on the peptide nanofibers with orientation. The cells have a prominent axis orientated about 0° (**Figure 4.13 A, B, C**) and +45° (**Figure 4.13 D-I**), suggesting a highly aligned cell arrangement on the peptide nanofibers on $K_2(SL)_6K_2$, $K_2(SL)_6K_2$NAP and $K_2(SL)_6K_2$NAV respectively.

In consideration of the encouraging outcomes in cell alignment, we investigated the potential of peptide nanofiber in directing the neuronal differentiation of hMSCs cells. We investigated the neuronal differentiation of hMSCs cells using solely biophysical and topographical cues (peptide nanofibers) without including retinoic acid (RA) in the treatment media. We observed the formation of elongated neurites and expression of mature neuronal maker MAP-2, confirming neuronal differentiation of hMSCs cells (**Figure 4.13 J, K**).

Collectively, the designed peptide nanofibers are the optimized scaffold in promoting the neuronal differentiation of hMSCs cells with the oriented arrangement and neural network formation. This suggests that the hydrogel has promise for use in regenerative medicine applications, particularly in facilitating tissue repair and regeneration (**Figure 4.14**).

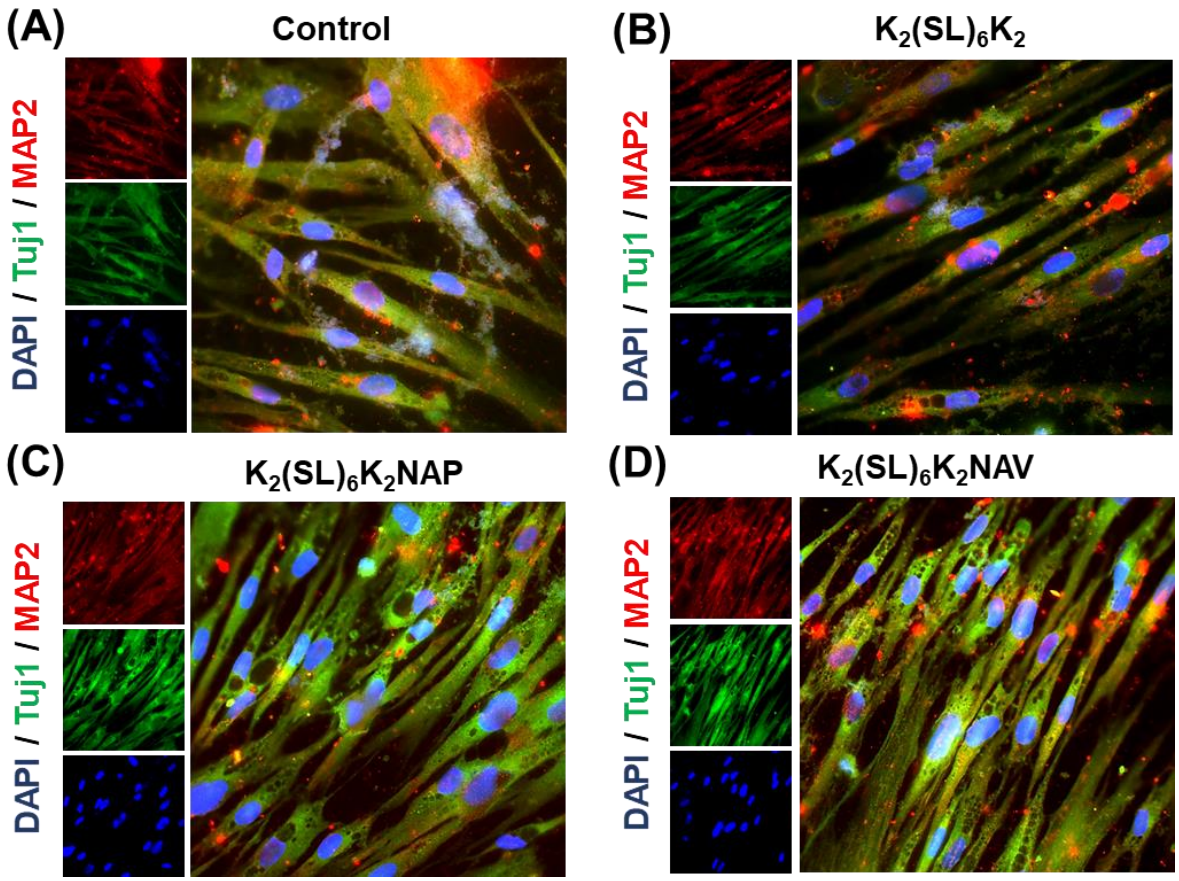


Figure 4.14: Differentiation of hMSCs derived neurons on different peptide hydrogel. Fluorescent images of the hMSCs derived neurons cells with the induction of differentiation for 7 days with different treatment conditions Control (A), $K_2(SL)_6K_2$ (B), $K_2(SL)_6K_2$NAP (C) and $K_2(SL)_6K_2$NAV (D).

4.4.7 Biomimetic MDPs Promote Neurite Outgrowth *In Vitro*: Peripheral nerves exhibit regenerative responses against any damage. In close proximity to the damage site, neurons initiate intrinsic signalling pathways that are controlled by transcriptional factors and facilitate the formation of nerve fibres. This state is characterized by enhanced neurite outgrowth, proliferation, migration, production of neurotrophic factors, and deposition of basal lamina proteins. Moreover, the technique of in vitro neurite outgrowth experiments has been effective in identifying genetic factors that regulate axon regeneration, as well as identifying pharmacological compounds that promote neuronal regeneration. A primary objective in treatment approaches for peripheral nerve injury is to enhance the rate of neurite outgrowth. In screening assays, in vitro estimation of neurite outgrowth is employed as a substitute measure to mimic the extension of neuronal processes *in vivo*. Hence, our initial objective is to assess the capacity of our designed peptide nanofibers to enhance neuronal regeneration.

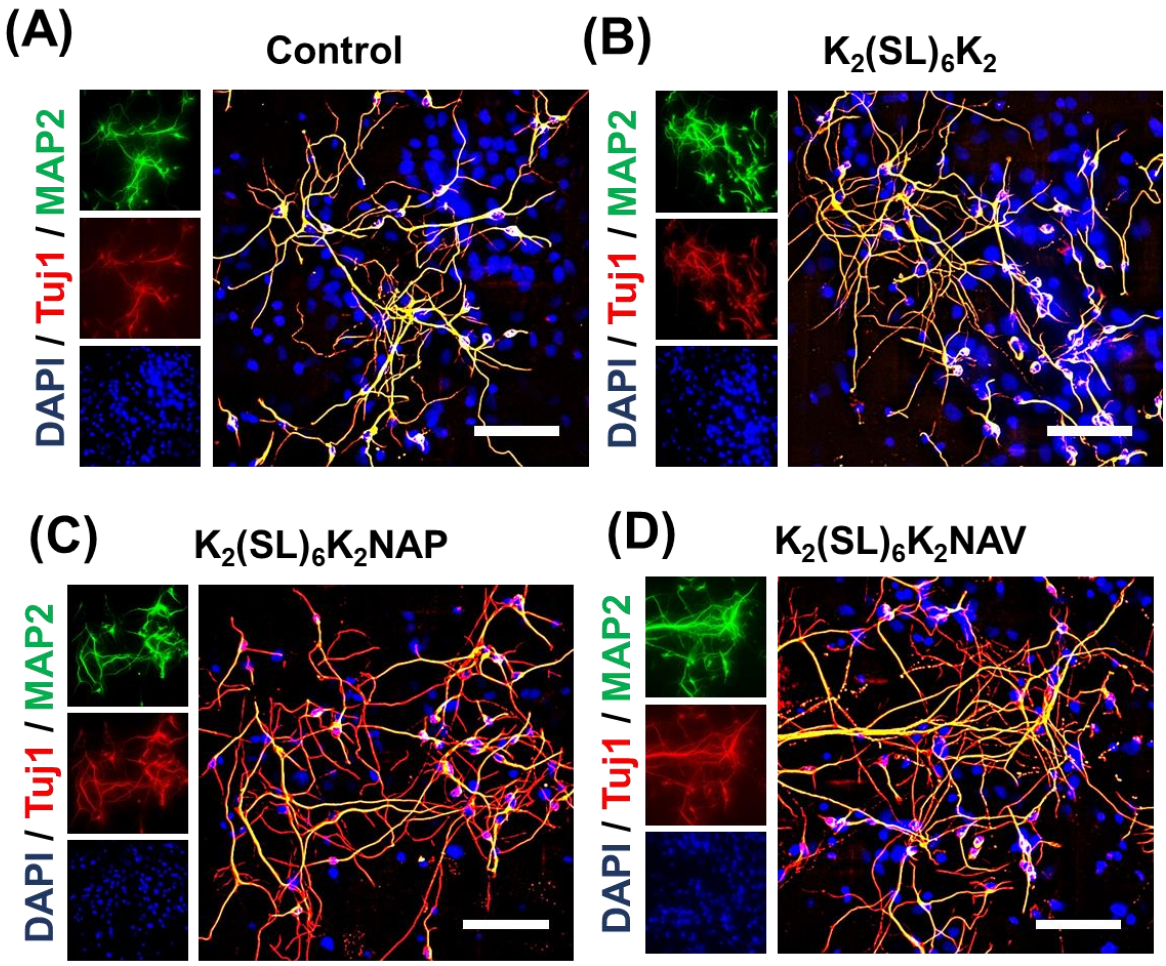


Figure 4.15. ICC of E18 primary cortical neurons stained with TUJ1, MAP2 and counter stained with Hoechst 33342, under (A) control condition and when treated with $K_2(SL)_6K_2$ (B), $K_2(SL)_6K_2$NAP (C), $K_2(SL)_6K_2$NAV (D). Scale bar corresponds to 50 µm.

The bioactivity of different peptide nanofibers in promoting neurite outgrowth was assessed using primary neuron culture, as previously reported. Primary neurons were seeded onto glass coverslips coated with different peptide nanofibers ($K_2(SL)_6K_2$, $K_2(SL)_6K_2$NAP and $K_2(SL)_6K_2$NAV). PDL-coated surfaces were used as an appropriate positive control. Neuronal cell morphologies were stained with Tuj1 and the extensive neurite tracings were stained with MAP2. These two markers have been frequently employed to quantify neuronal expansion in vitro and have been utilized to find factors that regulate axon regeneration (**Figure 4.15 A-D**).

The degree of neurite outgrowth on different peptide nanofibers was measured and compared to the outgrowth on the control surface. After 8-9 days of incubation, there was a noticeable rise in the neurite outgrowth when cells were placed on surfaces coated with peptide nanofibers. This was evident from the highly branching shapes observed, which were more pronounced compared to neurons grown on the standard PDL material.

The neurosphere generated from primary neuronal culture offers a new model that closely resembles the in vivo brain. Their use spans several domains of neuroscience research, including neurotoxicology assessments, investigations of cellular differentiation, and the modelling of neurodegenerative disorders. Consequently, to achieve this goal, we developed a neurosphere model to evaluate the effectiveness of our peptide hydrogel in promoting neurosphere growth. As shown in **Figure 4.16 A-C**, all three types of hydrogel showed good biocompatibility in promoting the neurosphere generated by hMSCs. Further, we have also checked the FE-SEM images of the primary cortical neurosphere grown on the $K_2(SL)_6K_2NAV$ hydrogel, and it also showing good morphology and shape (**Figure 4.16 C-D**).

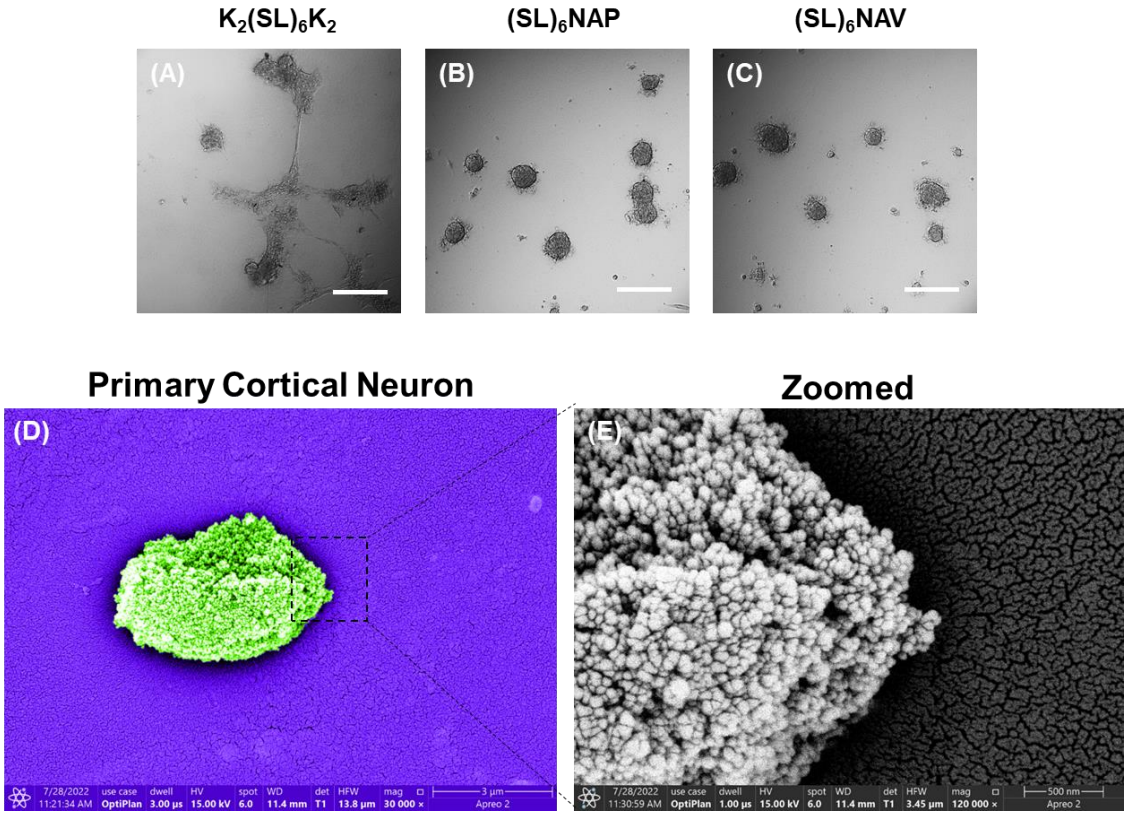


Figure 4.16: Generation of neurosphere. Generation of hMSCs derived neurosphere on different peptide hydrogels $K_2(SL)_6K_2$ (A), $K_2(SL)_6K_2NAP$ (B) and $K_2(SL)_6K_2NAV$ (C) for 7 days. Scale bar corresponds to 200 µm. (D) and (E) SEM image of Generation of neurosphere from primary cortical neuron. Scale bar corresponds to 3 µm in (D) and 500 nm in (E).

4.4.8 Histological Analysis of Nerve Regeneration: In order to assess the bioactivity of the peptide nanofibrous hydrogel *in vivo*, we conducted a sciatic nerve crush experiment. This experimental framework is commonly employed to investigate the regeneration response in the peripheral nervous system (PNS). Crushing of the sciatic nerve results in the destruction of all axons and myelin sheaths while leaving the epineurium and basal lamina intact, which aid in the process of nerve regeneration. Following nerve crush, a 10 µL hydrogel was delivered directly into the epineurium via direct injection, eliminating the requirement for conduits or autografts. This

approach facilitated the precise distribution of the peptide nanofibrous to the site of injury, enhancing specific regeneration and reducing the likelihood of unintended effects in other areas.

At 2 weeks post-surgery, regenerative nerve samples were collected from SNI rats and subjected to analysis using H&E. Longitudinal semi-thin sections of nerve samples were stained with H&E to examine the overview of the nerve tissue regeneration in response of the damaged nerves. As shown in **Figure 4.17 (A-F),** compression of the sciatic nerve results in the destruction of all axons and myelin sheaths, although the epineurium and basal lamina remain intact, which helps in the process of nerve regeneration. However, treatment with $K_2(SL)_6K_2NAV$ resulted in the regeneration of nerve fibers as seen with the increase in nerve fiber width. The sections from the $K_2(SL)_6K_2NAV$ exhibited a substantial and statistically significant enhancement compared to the sections from the $K_2(SL)_6K_2$, $K_2(SL)_6K_2NAP$ and matrigel groups (**Figure 4.17 C-F**). Moreover, sections from the $K_2(SL)_6K_2NAV$ group exhibited noticeably more pronounced fascicular areas. Thus, to check the effect of peptide hydrogel in alleviating the peripheral nerve injury the gastrocnemius muscle sections were stained to evaluate the changes facilitated by the peptide hydrogel.

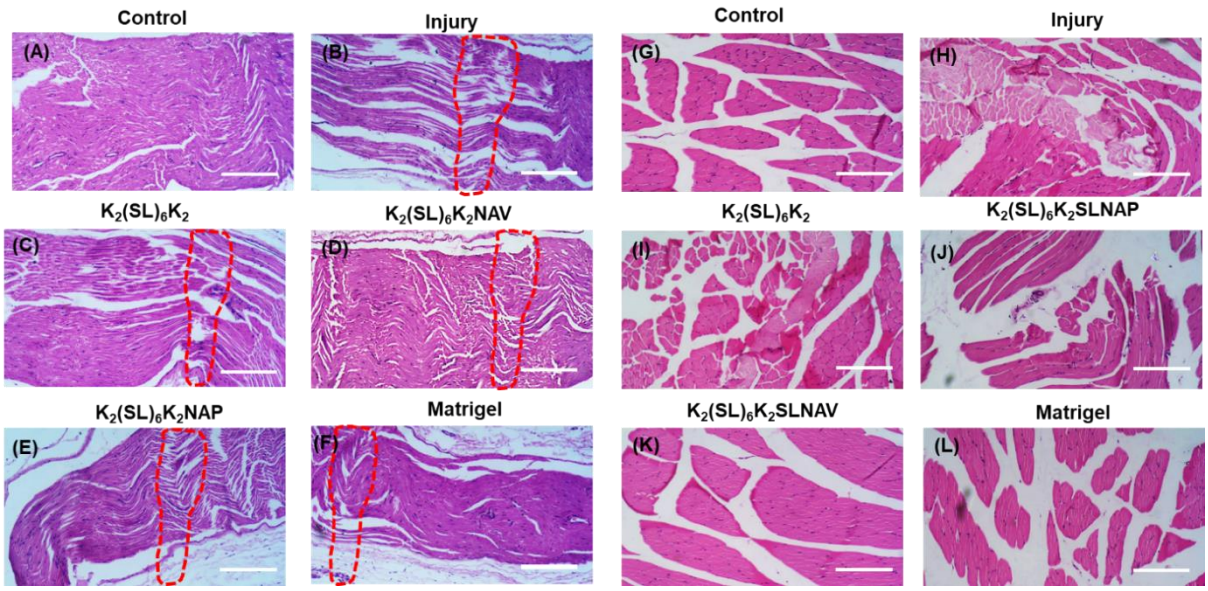


Figure 4.17 Structural methodology for assessing nerve tissue regeneration following crush injury. (A-F) Bright-field images of HE-stained transverse sections of sciatic nerves of rats belonging to different groups: control (A), sham-operated (B), $K_2(SL)_6K_2$ (C), $K_2(SL)_6K_2NAP$ (D) $K_2(SL)_6K_2NAV$ (E) and matrigel (F). Bright-field images of HE-stained cross section of gastrocnemius muscle belonging to different groups: control (G), sham-operated (H), $K_2(SL)_6K_2$ (I), $K_2(SL)_6K_2NAP$ (J) $K_2(SL)_6K_2NAV$ (K) and matrigel (L). Scale bar corresponds 200 µm.

4.4.9 Peptide Hydrogel Attenuated Gastrocnemius Muscle Atrophy in Peripheral Nerve Injury Rats: The sciatic nerve innervates the gastrocnemius muscle, which is crucial for the locomotion of the rat's hind limbs. Muscle atrophy is a common consequence of losing control over the nerves that regulate the muscle. Moreover, monitoring changes in muscle size can also provide valuable insights into the progression of recovery and guide further therapeutic strategies. Therefore, the extent of gastrocnemius muscle

atrophy can be used as an objective measure for determining the level of functional recovery from peptide hydrogel after a nerve injury. Hence, we used this method to assess quantitatively the effectiveness of peptide hydrogel in restoring nerve function. As shown in the **Figure 4.17 G-L,** the H and E staining of the transverse sections of the middle section of the gastrocnemius muscle showed that the muscle fibers in the injury group **(Figure 4.17 H**) were thinner and had a significantly smaller area ratio compared to the $K_2(SL)_6K_2$, $K_2(SL)_6K_2$NAP and $K_2(SL)_6K_2$NAV treatment and matrigel groups (**Figure 4.17 I-L**). One thing to note here is that $K_2(SL)_6K_2$NAV shows much better and large muscle fibers as compared to the injury group which signifies that $K_2(SL)_6K_2$NAV helps in tissue regeneration.

Gastrocnemius muscles were isolated and weighed 2 weeks following surgery. The experimental side gastrocnemius muscle in rats in the injury groups, $K_2(SL)_6K_2$NAP, $K_2(SL)_6K_2$NAV group and matrigel group displayed varying degrees of atrophy. Figure S14C shows the wet muscle weights of all the groups following different peptide hydrogel treatments after SCI. The $K_2(SL)_6K_2$NAP and $K_2(SL)_6K_2$NAV group had a significantly superior muscle wet weight, which signifies better recovery than the $K_2(SL)_6K_2$ group, but $K_2(SL)_6K_2$NAV group showed significantly much better result as compared to the $K_2(SL)_6K_2$NAP group which are similar to that of matrigel group.

4.4.10 Behavioral Assessment: Further, in order to determine the extent to which the peptide hydrogel resulted in functional improvement, we assessed the sciatic functional index (SFI), an index that indicates the degree of the sciatic nerve dysfunction, which was calculated at different time points for two weeks following the injury using empirical equations (**Figure 4.18 B**). By the end of second week, animals who were treated with peptide nanofibrous hydrogel had a noticeably higher SFI score compared to animals that were given saline treatment (**Figure 4.18 C**). The SFI of the peptide hydrogel group was significantly higher than that of the saline group and similar to that of the matrigel nerve implantation group at 2 weeks after the surgery. This suggests that the peptide hydrogel conduit will result in a satisfactory recovery of sciatic function.

Moreover, recording the footprints of rats and analysing their walking pattern are often used methods to evaluate the restoration of motor nerve function following peripheral nerve injury (PNI). This footprint analysis technique can offer valuable insight into the efficacy of different treatments and interventions designed to restore nerve function. Hence, we analysed the changes in gait and foot imprints to assess improvements in motor coordination and muscle strength over time for two weeks. For that case, we recorded the footprints of rats and analysed their walking pattern is a typical practice for evaluating the restoration of motor nerve function. In comparison to the control group, the footprints of the saline-treated group had a reduced depth, and the toes were tightly curled. However, the peptide treatment groups ($K_2(SL)_6K_2$, $K_2(SL)_6K_2$NAP, $K_2(SL)_6K_2$NAV) showed a noticeable enhancement and the animal foot was less intact in the injury group compared to the treatment group (**Figure 4.18 D**).

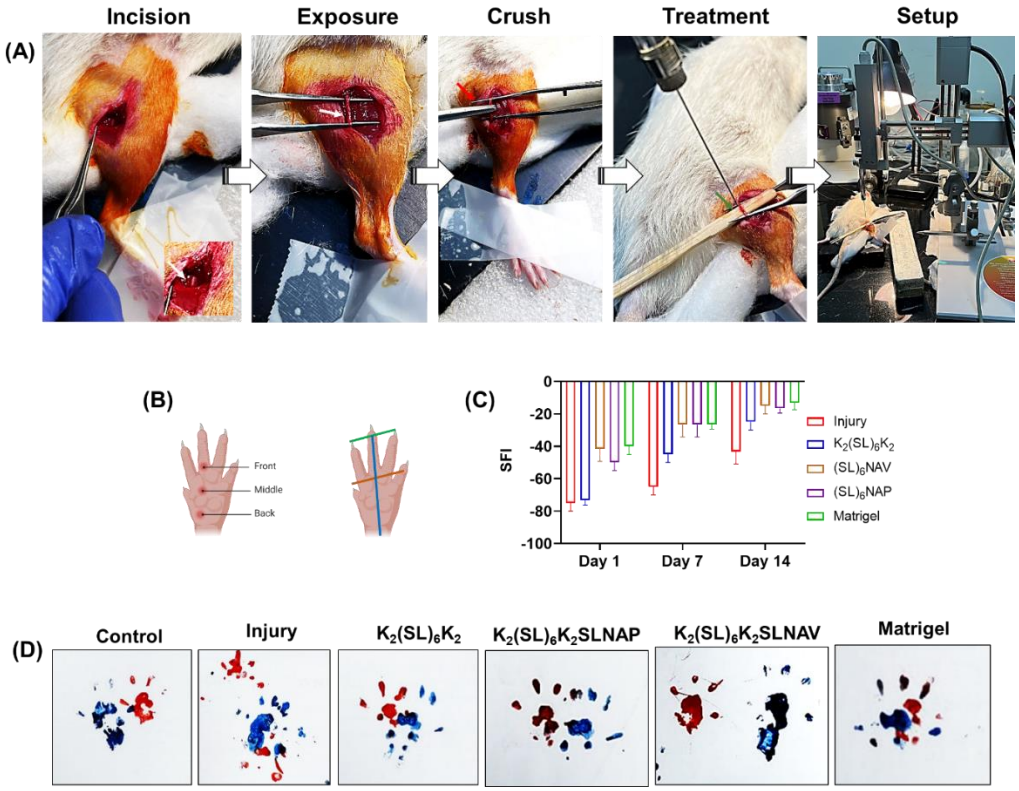


Figure 4.18 Representative images of (A) Sciatic crush nerve injury model generation with different steps and treatment administration. (B) Representative images of the rat footprint in calculating the SFI (C) Effect of different treatment group on SFI under crush injury and different treatment group. (D) Effect of different treatment group on SFI walking tract footprints under crush injury and different treatment groups. Data are represented as the mean ± s.d. from three independent experiments.

4.4.11 Functional Evaluation of Nerve Regeneration: There are a broad variety of motor tests that can be used to find motor deficits in animal models following SNI. One such test is the "beam walking test" or "balance beam test" which analyses the rodents walking pattern in a narrow beam and requires the animals to walk through a raised beam with a narrow diameter. Animals exhibiting weak motor coordination due to nerve injury struggle to traverse the beam and frequently make errors during the beam crossing, while healthy animals can easily cross the beam without making any errors.

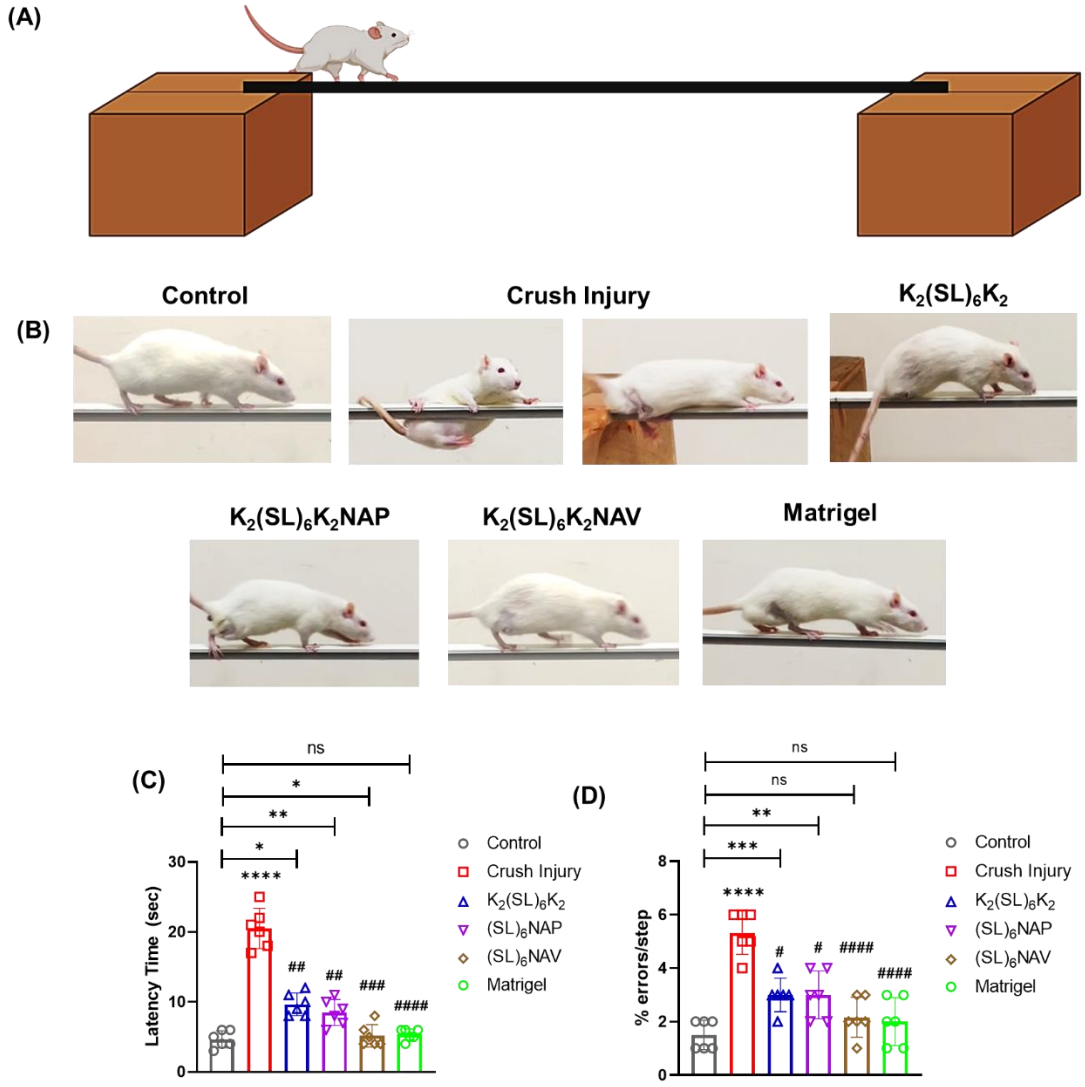


Figure 4.19 Schematic illustration of the (A) beam walking test to evaluate the functional recovery following nerve regeneration. (B) Representative images of the rat performance in the beam walking test under crush injury, different treatment conditions $K_2(SL)_6K_2$, $K_2(SL)_6K_2NAP$ and $K_2(SL)_6K_2NAV$ and positive control matrigel. (C) Typical cross time of different treatment groups to cross the group. (D) Foot slip errors per step of the crush injury, different treatment group during the beam walking task, broken down by percentage. Data are represented as the mean ± s.d. from three independent experiments. Significances are marked as *P< 0.05, **P< 0.01, **** P < 0.0001 versus the control group, ##P<0.05, ##P<0.01 #### P < 0.0001 versus the crush injury group.

Hence, we performed a beam walking analysis to analyze the effect of peptide hydrogel on ameroliating motor deficits in SCI (**Figure 4.19 A**). Videos were used to physically record the time needed to cross the beam, and the number of slips and falls (**Figure 4.19 B**). At 15 days after surgery, the saline treatment group took longer to get to cross the beam (20.5 s ± 2.62 s; $p < 0.05$) as compared to the peptide treatment $K_2(SL)_6K_2$ (9.66 s ± 1.49 s; $p < 0.0005$) group, $K_2(SL)_6K_2NAP$ (8.50 s ± 1.74 s; $p < 0.0005$), $K_2(SL)_6K_2NAV$ (5.16 s ± 1.46 s; $p < 0.0005$), and matrigel group (5.3 s ± 0.74 s; $p < 0.05$) (**Figure 4.19 C**). The $K_2(SL)_6K_2NAP$ and $K_2(SL)_6K_2NAV$ group showed much better results as compared to the only $K_2(SL)_6K_2$ group, which might be due to the effect of

NAP and NAV peptide groups. Further, we have also calculated the errors (slips and falls) that rats make while crossing the beam, and as expected, the saline treatment group showed a high number of error in crossing the beam as compared to the peptide hydrogel treatment group and matrigel group (**Figure 4.19 D**). Hence, both the parameters that we looked at did show statistically significant changes between the peptide hydrogel treatment and the saline treatment group.

Abbreviation	Peptide Sequence	Mimicking	Bioactivity
$K_2(SL)_6K_2$	$K_2(SL)_6K_2$	Neuroprotective	Neurite Outgrowth
$K_2(SL)_6K_2$NAP	$K_2(SL)_6K_2$**NAPVSIPQ**	ADNF	Stabilize Microtubule /Neurite Outgrowth
$K_2(SL)_6K_2$NAV	$K_2(SL)_6K_2$**NAPSIQ**	ADNF	Neuroprotective

Table 4.1 Peptide sequence of different SAMDPs

4.4.12 In Vivo Cytotoxicity Analysis: As part of a preliminary study, we did H&E labelling on important organs like the kidney, liver, spleen and lungs 15 days after treatment with different peptide nanofibers. This was done to see if the peptide hydrogel was compatible with these organs. The H and E results showed that there were no significant changes in the cellular organisation and appearance of different organs compared to the control group (**Figure 4.20**). This means that all the peptide hydrogel does not have any possible harmful effects in living things.

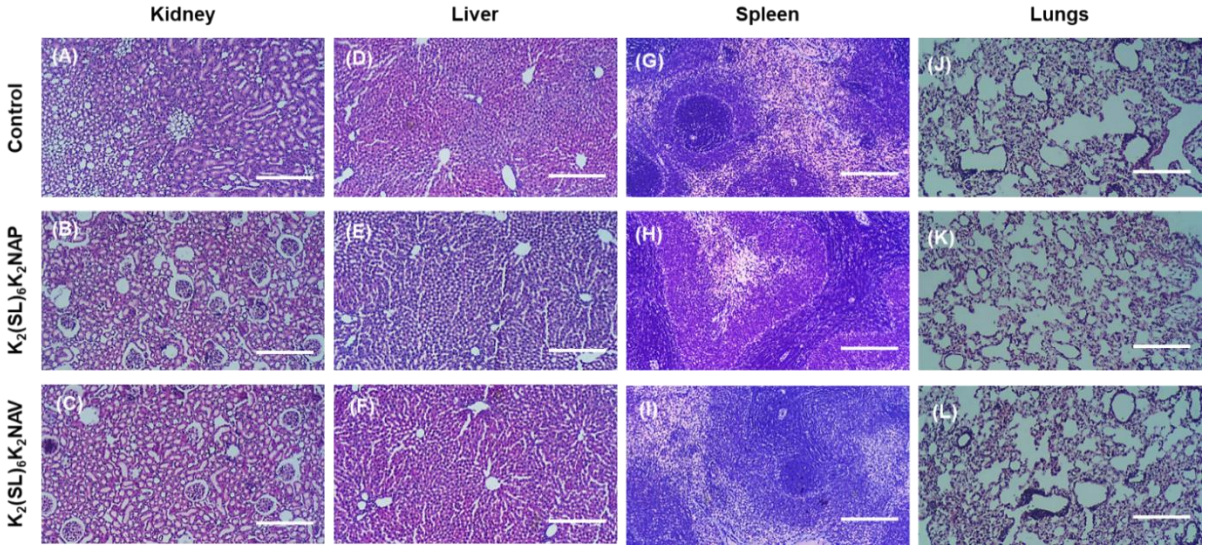


Figure 4.20 Representative images of the different organs harvested from the different peptide hydrogel treatment groups for the evaluation of *in vivo* cytotoxicity analysis (A-C) Shows the kidney H & E sections from control, $K_2(SL)_6K_2$, $K_2(SL)_6K_2$NAP and $K_2(SL)_6K_2$NAV group at the end of 14 days respectively, (D-F) Shows the liver H & E sections from control, $K_2(SL)_6K_2$, $K_2(SL)_6K_2$NAP and $K_2(SL)_6K_2$NAV group at the end of 14 days respectively (G-I) Shows the spleen H & E sections from control, $K_2(SL)_6K_2$, $K_2(SL)_6K_2$NAP and $K_2(SL)_6K_2$NAV group at the end of 14 days respectively, (J-L) Shows the kidney H & E sections from control, $K_2(SL)_6K_2$, $K_2(SL)_6K_2$NAP and $K_2(SL)_6K_2$NAV group at the end of 14 days respectively. The scale bar corresponds to 200 µm.

4.5 CONCLUSION

Although conventional neural conducts are commonly employed in clinics for SCI, they are accompanied by significant limitations that impede their efficacy in combating the problem of regeneration. To address this issue, we have developed two different self-assembling multi-domain peptide hydrogels by adding K_2 to the neuroprotective NAP and NAV peptides, which share a structural similarity with the active component of ADNF-9 for neural cell regeneration in SCI. The addition of these peptides induces the hydrogenation property in the hydrogel. The designed peptide hydrogel can help in the orientation and differentiation of hMSCs into neurons. Further, the designed peptide hydrogel is highly biocompatible with different fibroblast cell lines (WI-38, C2C12)

Overall, these designed peptide hydrogel conduits give greater functional recovery than untreated, negative control group 2 weeks postoperative, as indicated in H and E staining of sciatic nerves, gastrocnemius muscle, and gastrocnemius muscle weight. Further, these results were consistent with the regular behavioral assessment where NAP peptide hydrogel provides the best functional recovery. Hence we propose that this strategy of using peptide hydrogel would be highly useful for the design of further advanced therapeutics for the SCI.

4.6 REFERENCE

(1) Robinson, L. R. AAEM Minimonograph# 28: Traumatic Injury to Peripheral Nerves. *Rochester Am. Assoc. Electrodiagn. Med.* **2000**, 1–11.

(2) Taylor, C. A.; Braza, D.; Rice, J. B.; Dillingham, T. The Incidence of Peripheral Nerve Injury in Extremity Trauma. *Am. J. Phys. Med. Rehabil.* **2008**, *87* (5), 381–385.

(3) Ichihara, S.; Inada, Y.; Nakamura, T. Artificial Nerve Tubes and Their Application for Repair of Peripheral Nerve Injury: An Update of Current Concepts. *Injury* **2008**, *39*, 29–39.

(4) Lee, S. K.; Wolfe, S. W. Peripheral Nerve Injury and Repair. *JAAOS-Journal Am. Acad. Orthop. Surg.* **2000**, *8* (4), 243–252.

(5) Campbell, W. W. Evaluation and Management of Peripheral Nerve Injury. *Clin. Neurophysiol.* **2008**, *119* (9), 1951–1965.

(6) Lee, D. J.; Fontaine, A.; Meng, X.; Park, D. Biomimetic Nerve Guidance Conduit Containing Intraluminal Microchannels with Aligned Nanofibers Markedly Facilitates in Nerve Regeneration. *ACS Biomater. Sci. Eng.* **2016**, 2 (8), 1403–1410.

(7) Huang, C.; Ouyang, Y.; Niu, H.; He, N.; Ke, Q.; Jin, X.; Li, D.; Fang, J.; Liu, W.; Fan, C. Nerve Guidance Conduits from Aligned Nanofibers: Improvement of Nerve Regeneration through Longitudinal Nanogrooves on a Fiber Surface. *ACS Appl. Mater. Interfaces* **2015**, *7* (13), 7189–7196.

(8) Siemionow, M.; Brzezicki, G. Current Techniques and Concepts in Peripheral Nerve Repair. *Int. Rev. Neurobiol.* **2009**, *87*, 141–172.

(9) Manto, K. M.; Govindappa, P. K.; Parisi, D.; Karuman, Z.; Martinazzi, B.; Hegarty, J. P.; Talukder, M. A. H.; Elfar, J. C. (4-Aminopyridine)–PLGA–PEG as a Novel Thermosensitive and Locally Injectable Treatment for Acute Peripheral Nerve Injury. *ACS Appl. bio Mater.* **2021**, *4* (5), 4140–4151.

(10) Balint, R.; Cassidy, N. J.; Cartmell, S. H. Conductive Polymers: Towards a Smart Biomaterial for Tissue Engineering. *Acta Biomater.* **2014**, *10* (6), 2341–2353.

(11) Dwivedi, R.; Kumar, S.; Pandey, R.; Mahajan, A.; Nandana, D.; Katti, D. S.; Mehrotra, D. Polycaprolactone as Biomaterial for Bone Scaffolds: Review of Literature. *J. oral Biol. craniofacial Res.* **2020**, *10* (1), 381–388.

(12) Aldemir Dikici, B.; Reilly, G. C.; Claeyssens, F. Boosting the Osteogenic and Angiogenic Performance of Multiscale Porous Polycaprolactone Scaffolds by in Vitro Generated Extracellular Matrix Decoration. *ACS Appl. Mater. Interfaces* **2020**, *12* (11), 12510–12524.

(13) Dong, C.; Qiao, F.; Hou, W.; Yang, L.; Lv, Y. Graphene-Based Conductive Fibrous Scaffold Boosts Sciatic Nerve Regeneration and Functional Recovery upon Electrical Stimulation. *Appl. Mater. Today* **2020**, *21*, 100870.

(14) Garg, S.; Jana, A.; Khan, J.; Gupta, S.; Roy, R.; Gupta, V.; Ghosh, S. Logic "AND Gate Circuit" Based Mussel Inspired Polydopamine Nanocomposite as Bioactive Antioxidant for Management of Oxidative Stress and Neurogenesis in Traumatic Brain Injury. *ACS Appl. Mater. Interfaces* **2024**.

(15) Adak, A.; Das, G.; Khan, J.; Mukherjee, N.; Gupta, V.; Mallesh, R.; Ghosh, S. Extracellular Matrix (ECM)-Mimicking Neuroprotective Injectable Sulfo-Functionalized Peptide Hydrogel for Repairing Brain Injury. *ACS Biomater. Sci. Eng.* **2020**, *6* (4), 2287–2296.

(16) Pradhan, K.; Das, G.; Khan, J.; Gupta, V.; Barman, S.; Adak, A.; Ghosh, S. Neuro-Regenerative Choline-Functionalized Injectable Graphene Oxide Hydrogel Repairs Focal Brain Injury. *ACS Chem. Neurosci.* **2018**, *10* (3), 1535–1543.

(17) Adak, A.; Das, G.; Barman, S.; Mohapatra, S.; Bhunia, D.; Jana, B.; Ghosh, S. Biodegradable Neuro-Compatible Peptide Hydrogel Promotes Neurite Outgrowth, Shows Significant Neuroprotection, and Delivers Anti-Alzheimer Drug. *ACS Appl. Mater. Interfaces* **2017**, *9* (6), 5067–5076.

(18) Das, S.; Das, D. Rational Design of Peptide-Based Smart Hydrogels for Therapeutic Applications. *Front. Chem.* **2021**, *9*, 770102.

(19) Zhao, B.; Zhang, Q.; Yang, H.; Yu, S.; Fu, R.; Shi, S.; Wang, Y.; Zhou, W.; Cui, Y.; Guo, Q. Peptide KN-17-Loaded Supramolecular Hydrogel Induces the Regeneration of the Pulp-Dentin Complex. *ACS Biomater. Sci. Eng.* **2024**, *10* (4), 2523–2533.

(20) Lopez-Silva, T. L.; Cristobal, C. D.; Lai, C. S. E.; Leyva-Aranda, V.; Lee, H. K.; Hartgerink, J. D. Self-Assembling Multidomain Peptide Hydrogels Accelerate Peripheral Nerve Regeneration after Crush Injury. *Biomaterials* **2021**, *265*, 120401.

(21) Shi, P.; He, X.; Cong, H.; Yu, B.; Shen, Y. Preparation and Properties of Self-Assembling Polypeptide Hydrogels and Their Application in Biomedicine. *ACS Mater. Lett.* **2024**, *6* (5), 1649–1677.

(22) Hartgerink, J. D.; Beniash, E.; Stupp, S. I. Self-Assembly and Mineralization of Peptide-Amphiphile Nanofibers. *Science (80-.).* **2001**, *294* (5547), 1684–1688.

(23) Xie, C.; Chen, Y.; Wang, L.; Liao, K.; Xue, B.; Han, Y.; Li, L.; Jiang, Q. Recent Research of Peptide-Based Hydrogel in Nervous Regeneration. *Bioact. Mater.* **2024**, *40*, 503–523.

(24) Biswas, A.; Kurkute, P.; Saleem, S.; Jana, B.; Mohapatra, S.; Mondal, P.; Adak, A.; Ghosh, S.; Saha, A.; Bhunia, D. Novel Hexapeptide Interacts with Tubulin and Microtubules, Inhibits Aβ Fibrillation, and Shows Significant Neuroprotection. *ACS Chem. Neurosci.* **2015**, *6* (8), 1309–1316.

(25) Bassan, M.; Zamostiano, R.; Davidson, A.; Pinhasov, A.; Giladi, E.; Perl, O.; Bassan, H.; Blat, C.; Gibney, G.; Glazner, G. Complete Sequence of a Novel Protein Containing a Femtomolar-activity-dependent Neuroprotective Peptide. *J. Neurochem.* **1999**, *72* (3), 1283–1293.

(26) Dong, H.; Paramonov, S. E.; Aulisa, L.; Bakota, E. L.; Hartgerink, J. D. Self-Assembly of Multidomain Peptides: Balancing Molecular Frustration Controls Conformation and Nanostructure. *J. Am. Chem. Soc.* **2007**, *129* (41), 12468–12472.

(27) Moore, A. N.; Hartgerink, J. D. Self-Assembling Multidomain Peptide Nanofibers for Delivery of Bioactive Molecules and Tissue Regeneration. *Acc. Chem. Res.* **2017**, *50* (4), 714–722.

(28) Mallesh, R.; Khan, J.; Gharai, P. K.; Arshi, M. U.; Garg, S.; Gupta, S.; Ghosh, S. Hydrophobic C-Terminal Peptide Analog Aβ31–41 Protects the Neurons from Aβ-Induced Toxicity. *ACS Chem. Neurosci.* **2024**.

(29) Mondal, P.; Das, G.; Khan, J.; Pradhan, K.; Ghosh, S. Crafting of Neuroprotective Octapeptide from Taxol-Binding Pocket of β-Tubulin. *ACS Chem. Neurosci.* **2017**, *9* (3), 615–625.

(30) Pradhan, K.; Das, G.; Gupta, V.; Mondal, P.; Barman, S.; Khan, J.; Ghosh, S. Discovery of Neuroregenerative Peptoid from Amphibian Neuropeptide That Inhibits Amyloid-β Toxicity and Crosses Blood–Brain Barrier. *ACS Chem. Neurosci.* **2018**, *10* (3), 1355–1368.

(31) Pradhan, K.; Das, G.; Gupta, V.; Mondal, P.; Barman, S.; Khan, J.; Ghosh, S. Discovery of Neuroregenerative Peptoid from Amphibian Neuropeptide That Inhibits Amyloid-β Toxicity and Crosses Blood-Brain Barrier. *ACS Chem. Neurosci.* **2019**, *10* (3), 1355–1368. https://doi.org/10.1021/acschemneuro.8b00427.

(32) Khan, J.; Das, G.; Gupta, V.; Mohapatra, S.; Ghosh, S.; Ghosh, S. Neurosphere Development from Hippocampal and Cortical Embryonic Mixed Primary Neuron Culture: A Potential Platform for Screening Neurochemical Modulator. *ACS Chem. Neurosci.* **2018**, *9* (11), 2870–2878.

(33) Martinotti, S.; Ranzato, E. Scratch Wound Healing Assay. *Epidermal cells methods Protoc.* **2020**, 225–229.

(34) Iqbal, M. H.; Revana, F. J. R.; Pradel, E.; Gribova, V.; Mamchaoui, K.; Coirault, C.; Meyer, F.; Boulmedais, F. Brush-Induced Orientation of Collagen Fibers in Layer-by-Layer Nanofilms: A Simple Method for the Development of Human Muscle Fibers. *ACS Nano* **2022**, *16* (12), 20034–20043.

(35) Gupta, V.; Gharai, P. K.; Kar, C.; Garg, S.; Ghosh, S. Ratiometric Fluorescent Probe Promotes Trans-Differentiation of Human Mesenchymal Stem Cells to Neurons. *ACS Chem. Neurosci.* **2024**, *15* (2), 222–229.

(36) Antonova, O. Y.; Kochetkova, O. Y.; Kanev, I. L.; Shlyapnikova, E. A.; Shlyapnikov, Y. M. Rapid Generation of Neurospheres from Hippocampal Neurons Using Extracellular-Matrix-Mimetic Scaffolds. *ACS Chem. Neurosci.* **2021**, *12* (15), 2838–2850.

(37) Sun, W.; Sun, C.; Lin, H.; Zhao, H.; Wang, J.; Ma, H.; Chen, B.; Xiao, Z.; Dai, J. The Effect of Collagen-Binding NGF-β on the Promotion of Sciatic Nerve Regeneration in a Rat Sciatic Nerve Crush Injury Model. *Biomaterials* **2009**, *30* (27), 4649–4656.

(38) Gigo-Benato, D.; Russo, T. L.; Geuna, S.; Domingues, N. R. S. R.; Salvini, T. F.; Parizotto, N. A. Electrical Stimulation Impairs Early Functional Recovery and Accentuates Skeletal Muscle Atrophy after Sciatic Nerve Crush Injury in Rats. *Muscle Nerve Off. J. Am. Assoc. Electrodiagn. Med.* **2010**, *41* (5), 685–693.

(39) Luong, T. N.; Carlisle, H. J.; Southwell, A.; Patterson, P. H. Assessment of Motor Balance and Coordination in Mice Using the Balance Beam. *J. Vis. Exp. JoVE* **2011**, No. 49.

(40) Kanaya, F.; Firrell, J. C.; Breidenbach, W. C. Sciatic Function Index, Nerve Conduction Tests, Muscle Contraction, and Axon Morphometry as Indicators of Regeneration. *Plast. Reconstr. Surg.* **1996**, *98* (7), 1264–1271.

(41) Zhang, H.; Lan, D.; Wu, B.; Chen, X.; Li, X.; Li, Z.; Dai, F. Electrospun Piezoelectric Scaffold with External Mechanical Stimulation for Promoting Regeneration of Peripheral Nerve Injury. *Biomacromolecules* **2023**, *24* (7), 3268–3282.